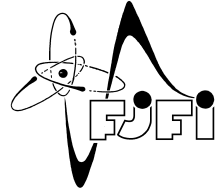




CZECH TECHNICAL UNIVERSITY IN PRAGUE
Faculty of Nuclear Sciences and Physical
Engineering



Reconstruction of Cell Images Acquired by Super-resolution Microscopy

Rekonstrukce snímků buněk pořízených pomocí mikroskopie se strukturovaným osvětlením

Bachelor's Degree Project

Author: **Martin Kunz**
Supervisor: **doc. Ing. Filip Šroubek, Ph.D. DSc.**
Consultant: **Dr. Zuzana Kadlecová**
Academic year: 2023/2024

ZADÁNÍ BAKALÁŘSKÉ PRÁCE

| | |
|-------------------------|--|
| Student: | Martin Kunz |
| Studijní program: | Aplikace přírodních věd |
| Studijní obor: | Matematické inženýrství |
| Studijní zaměření: | Aplikované matematicko-stochastické metody |
| Název práce (česky): | Rekonstrukce snímků buněk pořízených pomocí mikroskopie se strukturovaným osvětlením |
| Název práce (anglicky): | Reconstruction of Cell Images Acquired by Super-resolution Microscopy |

Pokyny pro vypracování:

- 1) Seznamte se se současnými automatickými metodami na sledování buněčného procesu endocytózy v časosběrných snímcích pořízených TIRF (total internal reflection fluorescence) mikroskopem. Výsledkem metod je detekce a sledování endocytózy v čase.
- 2) Nastudujte principy mikroskopie se strukturovaným osvětlením a rekonstrukční metody SIM (structured illuminated microscopy), které vytváří snímek s násobným rozlišením pomocí rekonstrukcí snímků osvětlených modulovaným, strukturovaným laserovým paprskem.
- 3) Navrhněte metody na odhad impulzní odezvy mikroskopu (Point Spread Function). Experimentálně ověřte vliv prostorové proměnnosti této odezvy.
- 4) Zaintegrujte odhady PSF do stávajících optimalizačních metod provádějící rekonstrukci SIM snímků.
- 5) Proveďte experimentální validaci navržených metod na synthetický i reálných datech.



Martin Kunz

Doporučená literatura:

- 1) C. M. Bishop, Pattern Recognition and Machine Learning. Springer, 2006.
- 2) R. C. Gonzales, R. E. Woods, Digital Image Processing (2nd ed.). Prentice Hall, 2002.
- 3) B. Zitová, J. Flusser, Image registration methods: a survey. Image and Vision Computing 21(11), 2003, 977-1000.
- 4) F. Aguet, C. N. Antonescu, M. Mettlen, S. L. Schmid, G. Danuser, Advances in analysis of low signal-to-noise images link dynamin and AP2 to the functions of an endocytic checkpoint. Developmental cell 26(3), 2013, 279-291.

Jméno a pracoviště vedoucího bakalářské práce:

doc. Ing. Filip Šroubek, Ph.D. DSc.

Oddělení zpracování obrazu, Ústav teorie informace a automatizace AV ČR, Pod Vodárenskou věží 4, 182 08 Praha 8

Jméno a pracoviště konzultanta:

Dr. Zuzana Kadlecová / Ing. Tomáš Kerepecký

Cambridge Institute for Medical Research, University of Cambridge, United Kingdom , / ,
Oddělení zpracování obrazu, Ústav teorie informace a automatizace AV ČR, Pod Vodárenskou věží 4, 182 08 Praha 8

Datum zadání bakalářské práce: 31.10.2022

Datum odevzdání bakalářské práce: 2.8.2023


Doba platnosti zadání je dva roky od data zadání.

V Praze dne 31.10.2022


.....
garant oboru


.....
vedoucí katedry




.....
děkan

Acknowledgment:

I would like to thank doc. Ing. Filip Šroubek, Ph.D. DSc. for his expert guidance and uninterrupted patience during the implementation of methods from image processing and writing of the thesis. It has been an honour to be able to discuss ideas and possibilities with him and I am very grateful for his advice and direction throughout the duration of the whole project. I am aware that at some times it must have been very hard to supervise me and point me to the correct path, but with his help and acquired wisdom, he has managed to make my time during the project a lot more manageable and enjoyable.

I would also like to thank my supervisor, Dr. Zuzana Kadlecová, for her explanations of biological aspects of endocytosis and her enthusiastic attitude, which on occasion prevented me from losing motivation.

An appreciation is also appropriate for Mgr. Adam Harmanec who has been always there with offers of help and advice in the implementation of the algorithms. The time spent by him whilst debugging and verification of results has been of immense value to me and I am very grateful.

My genuine "thank you" goes out to all three of you! I have learned a lot in this time and you all have contributed in this manner. It has been a pleasure and an honour to work with you.

Author's declaration:

I declare that this Bachelor's Degree Project is entirely my own work and I have listed all the used sources in the bibliography.

Prague, Tuesday 9th January, 2024

Martin Kunz

Název práce:

Rekonstrukce snímků buněk pořízených pomocí mikroskopie se strukturovaným osvětlením

Autor: Martin Kunz

Obor: Matematické inženýrství

Zaměření: Aplikované matematicko-stochastické metody

Druh práce: Bakalářská práce

Vedoucí práce: doc. Ing. Filip Šroubek, Ph.D. DSc., Oddělení zpracování obrazu, Ústav teorie informace a automatizace AV ČR, Pod Vodárenskou věží 4, 182 08 Praha 8

Konzultant: Dr. Zuzana Kadlecová, Cambridge Institute for Medical Research, University of Cambridge, United Kingdom, / Oddělení zpracování obrazu, Ústav teorie informace a automatizace AV ČR, Pod Vodárenskou věží 4, 182 08 Praha 8

Abstrakt: Super-rozlišení (SR) je výkonná metoda pro pozorování, která nabízí významné zlepšení rozlišení jak v laterálním, tak axiálním směru dosahující daleko za difrakční limit standardního světelného mikroskopu. To vedlo k mnoha významným objevům v biologii během posledních 50-ti let od vzniku prvních metod SR. Mezi metody SR má mikroskopie se strukturovaným osvětlením (SIM) důležitou výhodu ve své flexibilitě implementace a fotonové efektivitě, díky které hraje vedoucí roli v akvizici živých buněk s vysokou frekvencí snímků.

Nejprve jsou prezentovány základní fyzikální principy nutné pro určení přenosu světla optickým mikroskopem, v podobě odvození vlnové rovnice pro elektro-magnetické (EM) pole spolu s jejími dvěma řešeními nejvýznamnějšími pro aplikaci v optice mikroskopu. Dále je představen přehled dostupných metod SR se zaměřením na srovnání jejich užití v biologických pozorováních. Intuitivní pojetí fungování mikroskopie se strukturovaným osvětlením je ilustrováno a následně matematicky představena podstata při harmonickém osvětlení. Pomocí přehledu příkladů využití SIMu v kombinaci s dalšími modalitami mikroskopie a v různých implementacích demonstrují flexibilitu této metody SR.

Poté je provedena analýza pozorování mikrokuliček z akvizice pomocí harmonického osvětlení s cílem vylepšit kvalitu rekonstrukce. Jsou odvozeny, implementovány a demonstrovány dvě různé metody rekonstrukce v několika variantách. Schopnost omezit počet akvizic potřebných pro rekonstrukci je diskutována a ukázána spolu s komentářem k dalším aspektům, výhodám a nevýhodám rekonstrukčních technik, které byly i nebyly použity.

Další zlepšení rekonstrukčních metod snižováním přítomnosti artefaktů a zlepšováním vizuální kvality a rozlišení je dosaženo rekonstrukcí s odhadovanou přenosovou funkcí optického systému. Odhad je proveden pomocí různých postupů využívajících model struktury vzorku, který určen vlastním novým algoritmem inspirovaným zavedenými metodami digitálního zpracování obrazu. Zvýšená věrnost rekonstrukce akvizice nad aktuálně používanou metodou pro rekonstrukci endocytózy na povrchu buněčné membrány je dosažena odhadem přenosové funkce řízené přímo daty z akvizice samotné.

Klíčová slova: mikroskopie se strukturovaným osvětlením, super-rozlišení, přenosová funkce

Title:

Reconstruction of Cell Images Acquired by Super-resolution Microscopy

Author: Martin Kunz

Abstract: Super-resolution (SR) is a powerful imaging approach which offers significant gains in both lateral and axial resolution far beyond the diffraction limit of standard wide-field microscopy. This has led to numerous breakthroughs in biology during the past 50 years of its existence. Among SR methods, structured illumination microscopy (SIM) has a major advantage with its flexibility of implementation and photon-efficiency due to which it plays a lead role in high-frequency *in vivo* cell acquisitions.

First the elementary physics necessary for determining the transfer of light through an microscope is given by the derivation of the electro-magnetic (EM) field wave equation along with two of its most significant solutions for the application of microscopy optics. Next an condensed but informative overview of available SR methods is presented with the focus on comparing their utility in biological sensing applications. Intuitive conception behind the functioning of SIM is illustrated before the mathematical presentation of the fundamentals of harmonic SIM. An enumeration of examples where SIM is used in combination with other microscopy modalities and in various implementations demonstrates the flexibility the technique.

Then an analysis of micro-beads images from a harmonic SIM acquisition is performed with the goal of enhancing the reconstruction. Two different methods of reconstruction are derived, implemented and demonstrated in multiple variations. The ability of limiting the number of acquisitions necessary for the reconstruction is discussed and shown alongside a commentary of further aspects, benefits and drawbacks of the reconstruction techniques.

Further enhancements to the reconstruction techniques in the reduction of artefacts and improvement of visual quality and resolution is achieved by performing them with an estimated transfer function of the optical system. The estimation is performed using various procedures utilizing the model of the source structure in the object space of the determined by a custom novel algorithm inspired by multiple digital image processing algorithms. The fidelity over the SIM imaging technique currently used for the reconstruction of endocytosis at the cell membrane surface is attained by the data-driven transfer function estimate.

Key words: structured illumination microscopy, super-resolution imaging, transfer function

Contents

| | |
|---|-----------|
| Contents | i |
| Introduction | 1 |
| | |
| THEORY | 3 |
| | |
| 1 Nature of Light | 4 |
| 1.1 Historical Context | 4 |
| 1.2 Wave Theory of Light | 5 |
| Wave Equation of Light | 6 |
| 1.3 Wave Equation Solutions | 6 |
| Spherical Wave | 7 |
| Planar Wave | 9 |
| Harmonic Waves | 11 |
| | |
| 2 Super-resolution Microscopy | 12 |
| 2.1 Comparison of SR Methods | 12 |
| 2.2 Principle of SIM | 15 |
| 2.3 SIM | 16 |
| 2.4 Discussion | 17 |
| | |
| EXPERIMENT | 19 |
| | |
| 3 SIM Reconstruction | 20 |
| 3.1 Parameter Estimation | 21 |
| Phase-shift Estimate | 22 |
| Phase-Offset and Modulation Estimate | 24 |
| 3.2 Wiener filter Reconstruction | 24 |
| Separation of Components (i.) | 25 |
| Shifting Components (ii. and iii.) | 25 |
| Wiener Filter (iv.) | 27 |
| Apodization | 28 |
| 3.3 Inversion Reconstruction | 29 |
| Forward Model | 29 |
| Loss Function | 30 |
| Regularization Term | 31 |
| Optimization | 31 |
| 3.4 Discussion | 32 |
| | |
| 4 Measurement of the Transfer Function | 35 |
| 4.1 Image Formation | 35 |
| Illumination | 35 |
| Noise | 36 |
| The Transfer Function | 39 |
| The Source | 40 |
| 4.2 point spread function (PSF) from Beads | 41 |
| 4.3 The Source Model | 43 |
| Single Bead Model (i.) | 43 |

| | |
|--|-----------|
| Locating the Beads (ii.) | 44 |
| 4.4 Estimating the PSF from the Model | 47 |
| 4.5 point spread function (PSF) from SIM | 47 |
| 4.6 New Reconstruction | 47 |
| 4.7 Discussion | 50 |
| Conclusion | 53 |
| Bibliography | 54 |

Introduction

Advancements in precise and accurate observation techniques have always been at the forefront of scientific endeavours. Novel approaches often lead to chains of revolutionary new discoveries in the fields that utilize these methods.

In microscopy, a physical limit that for a long time seemed unbreakable was *Abbe's* resolution limit, due to diffraction induced by the light transfer through the microscope. This bound, restricting both the lateral (≈ 180 nm) and the axial (≈ 450 nm) axes of resolution, remained a constraint for the precision of observation in microscopy for more than a century from its derivation, stifling progress in biology and countless other fields which depend on measurement and observation through microscopy imaging.

Hope for better resolving power was re-established by a breakthrough at the hands of the *Cremer* brothers in the mid 1970s by a revolutionary approach to microscopy observation ($4\pi M$) that led to the possibility of about 4-fold improvement in the axial resolution. This discovery incited a revolution, in which new methods were introduced at an unprecedented speed for this field. As a result of this rise of attention, not long after, methods for improving the more practicable lateral resolution were developed and implemented. These methods which outperform the physical limits of *Abbe* in at least one of the axes of resolution became collectively known as super-resolution (SR) methods. Most of these methods, however, relied on long acquisition times stemming from the necessity of sensing a narrow volume of the sample object field which deemed them unusable for applications with non-static specimen.

This pressing barrier for implementing SR for use in *in vivo* examination was overcome with a new technique in the mid 1990s which was based on significantly different principles within the optical acquisition than the previous methods. Improvements that built upon the presented aforementioned SIM method were rapidly developed and its implementation was widely adopted throughout the scientific community. Further methods that employed the principles of SIM also found their grounds in application. These two waves of research have resulted in the creation of a plethora of approaches and implementations of SR methods.

The original SIM technique is still very relevant in present-day and the reconstruction methods for it are continually improving. An underlying concept behind SIM is the transfer function, which is modulated by the *structured illumination* which the SIM method prescribes. With respect to this, the knowledge of the correct transfer function is fundamental to reconstruction techniques of the SIM method.

A transfer function is a powerful concept, which is not limited to microscopy. It is fundamental due to the fact that it fully determines the mapping of a linear system, which it represents. The utility of the knowledge of transfer functions is undeniable since physical systems are often linear or can be approximated by a linear system.

In the context of SIM, an incorrect transfer function, may lead to artefacts and undetermined fidelity of the reconstruction and so it is crucial to determine it correctly. With this in mind, there are two major approaches to deriving the transfer function of the optical system:

modeling Considers the context of the optical setup and the nature of the propagating light to determine an appropriate transfer function with the relevant aberrations of the lens system and aperture.

estimation Resorts to the sensed signal of an acquisition and through modeling the source signal which produced the result, infers an estimated transfer function.

I use the estimation approach to derive the applicable transfer function of our acquisition in approximation for the whole field and subsequently for the individual locations within the focal plane. I incorporate this estimate into the reconstruction procedure to achieve better results than were previously available for use in our analysis of endocytosis at the outer cell membrane.

THEORY

1

Nature of Light

| | |
|--------------------------------|----|
| 1.1 Historical Context | 4 |
| 1.2 Wave Theory of Light . . | 5 |
| Wave Equation of Light . . | 6 |
| 1.3 Wave Equation Solu- | |
| tions | 6 |
| Spherical Wave | 7 |
| Planar Wave | 9 |
| Harmonic Waves | 11 |

1: For instance, he conjectured that vision is formed by rays emanating from the observers eyes.

2: More commonly known by the latinized name in Europe as *Alhazen*.

3: This was further developed by *Johannes Kepler* in the 17th century, who suggested the concept of retinal images.

[1]: Raynaud (2016), *A Critical Edition of Ibn al-Haytham's On the Shape of the Eclipse: The First Experimental Study of the Camera Obscura*



Figure 1.1: Crescent shaped images formed during the solar eclipse when light passes through openings between the leaves of a tree.

4: This view has interestingly close properties to the way, light is described in present day optics.

[2]: Isaac Newton (1704), *Opticks, Or, A Treatise of the Reflections, Refractions, Inflections & Colours of Light*

To recognize the fundamental inherent limits present in optical sensing, it is important to understand the physical nature of the processed signal, light.

1.1 Historical Context

Light was perceived in many different ways throughout the history of human kind. The first major work that studied optics was written by *Euclid* in the 4th century BCE. It mainly dealt with the geometry of vision and did not study the physical aspects of light in much detail. However his views of light and vision were significantly different from ours¹. Optics as a field is often considered to have been commenced by *Hasan Ibn al-Haytham*² in the 11th century by his experimental work and the *Book of Optics*, which he wrote to summarize them. It introduced the idea that vision results from light entering our eyes through the retina as opposed to the other way around³. He also extensively studied the *camera obscura* phenomenon in his treatise *On the Shape of the Eclipse* in which he ventured to explain the crescent shaped images formed during an eclipse when light passes through a small aperture as can be seen in Figure 1.1 [1].

There have been many attempts to explain light during the middle ages, but more often than not, they were not in accordance with its known experimental properties. In particular, a notable idea was brought forward by *René Descartes* in the beginning of the 17th century, who described light as a propagating pressure in an unspecified medium⁴. In 1690 *Christiaan Huygens* introduces the *wave theory of light* in his work *Traité de la Lumière*. His major contribution was the conceptualization of light as a vibration in a medium and his methods of analysis are used even today termed as the *Huygens-Fresnel principle*. The first comprehensive theory of light that was widely adopted, can be dated back to *Sir Isaac Newton* at the start of the 18th century. *Newton* was aware of the wave theory of light but rejected it in favour of the *corpuscular theory*, which he laid the foundations to [2]. It states that light is composed of particles called *corpuscles* travelling in a straight line with finite velocity. By the rise of the corpuscular theory, the branch that we now call *geometrical optics*, which was earlier developed by *Alhazen* was markedly improved. The corpuscular theory and geometrical optics explained a mayor part of the conundrums that astronomers had about the optical instrumentation of that time and due to this it prevailed for a long time at the forefront of established theories of light.

However, for the recognition of the way light passes through and transforms in a microscope, or in fact any optical system that we use for observation, and especially to study the resolution that is possible to

achieve, it is necessary to advance to the later centuries and developments made in the wave theory of light. A radical shift towards the supremacy of the wave model explanation instead of light rays, was the famous *double-slit experiment* performed by *Thomas Young* in 1801, which leads to results that are in conflict with the sole explanation by the simpler corpuscular theory. Further mathematical structure to the notion of interference emerging from the double-slit experiment was given by *Augustin-Jean Fresnel*, who in 1818 was the first to give a satisfactory explanation of diffraction by a straight edge in the form of the *Fresnel integral*, which will be important for us in further sections. The brilliant mathematician *James Clerk Maxwell* later in 1873 gave a unified and robust theoretical framework for EM fields, which light is a manifestation of.

1.2 Foundations of the Wave Theory of Light

Maxwell's unification of the theory of EM fields came in the manner of twenty differential equations which were later condensed by *Oliver Heaviside* into the notorious forms of the four equations that are today known as *Maxwell's equations*. Given in their most general differential form in SI units, they are

$$\nabla \cdot \varepsilon \mathbf{E} = \rho, \quad (\text{Gauss's law for } \mathbf{E})$$

$$\nabla \cdot \mu \mathbf{B} = 0, \quad (\text{Gauss's law for } \mathbf{B})$$

$$\nabla \times \mathbf{E} = -\partial_t \mathbf{B}, \quad (\text{Faraday's law})$$

$$\nabla \times \mathbf{B} = \mu \mathbf{J} + \varepsilon \mu \partial_t \mathbf{E}, \quad (\text{Ampère-Maxwell's law})$$

where $\mathbf{E} = \mathbf{E}(\vec{r}, t)$ and $\mathbf{B} = \mathbf{B}(\vec{r}, t)$ are the electric and magnetic fields respectively, $\mathbf{J} = \mathbf{J}(\vec{r}, t)$ is the current density, $\rho = \rho(\vec{r})$ is the electric charge density, $\varepsilon = \varepsilon(\vec{r})$ and $\mu = \mu(\vec{r})$ are permittivity and permeability of the propagation medium respectively. These equations can be simplified for the case of the medium that is applicable to us [3]. As a first simplification, we assume the absence of free charges ($\rho \equiv 0$) and free currents ($\mathbf{J} \equiv 0$) which lead to the simplification of Gauss's law for \mathbf{E} and Ampère-Maxwell's law. We postulate a well-behaved *insulating (dielectric)* medium in its response to the electric field, where $\mathbf{D} = \varepsilon \mathbf{E} + \mathbf{P}$ is the electric displacement field and \mathbf{P} is the field of polarization, in the form of an assumption of *linearity* implying that the polarization \mathbf{P} is proportional to the electric field, that is $\mathbf{P} \propto \mathbf{E}$, *non-dispersiveness* meaning that the polarization $\mathbf{P}(t)$ is dependent on $\mathbf{E}(t)$ only at the same time instant, *local homogeneity* meaning that the dependence of \mathbf{P} on \mathbf{E} is the same at every point \vec{r} within a neighbourhood and *isotropy* meaning that the relation is identical for every direction of \mathbf{E} . In the terms of a medium within which the light propagates *non-dispersiveness* implies that $\varepsilon(\lambda) \equiv \text{const.}$ where λ is the wavelength of the propagating EM wave, *homogeneity* implies $\varepsilon(\vec{r}) \equiv \text{const.}$ in some neighbourhood and *isotropy* implies that $\varepsilon(\mathbf{E}/|\mathbf{E}|) \equiv \text{const.}$ so in all directions of the field, the permittivity is the same. Also the medium in optics is assumed to be *non-magnetic* and so $\mu \equiv \mu_0$, which is the permeability in vacuum. The applicable

[3]: Goodman (2005), *Foundations of Scalar Diffraction Theory*

simplified equations are

$$\begin{aligned}\nabla \cdot \mathbf{E} &= 0, & \nabla \cdot \mathbf{B} &= 0, \\ \nabla \times \mathbf{E} &= -\partial_t \mathbf{B}, & \nabla \times \mathbf{B} &= \varepsilon\mu_0 \partial_t \mathbf{E}.\end{aligned}\tag{1.1}$$

Notice that due to the *homogeneity*, the permittivity ε and permeability μ , no longer appear in Gauss's law for \mathbf{E} and \mathbf{B} in the simplified equations.

The Wave Equation for Light

The goal is to transform the equations of 1.1 to the wave equation for both \mathbf{E} and \mathbf{B}

$$\nabla^2 \Psi - \frac{\partial_t^2 \Psi}{v^2} = 0, \quad (\square_v \Psi)$$

where v is the waves propagation speed. For \mathbf{E} , this can be done starting from Faraday's law in the simplified form (Eq. (1.1)) by applying the curl operation to both sides [4]. Customarily, starting from Faraday's law, we get for the left side

$$\nabla \times (\nabla \times \mathbf{E}) = \nabla(\nabla \cdot \mathbf{E}) - \nabla^2 \mathbf{E} = -\nabla^2 \mathbf{E},$$

where we used, in order, the *curl of curl* identity and Gauss's law for \mathbf{E} and for the right side

$$-\nabla \times (\partial_t \mathbf{B}) = -\partial_t (\nabla \times \mathbf{B}) = -\partial_t (\varepsilon\mu_0 \partial_t \mathbf{E}) = -\varepsilon\mu_0 \partial_t^2 \mathbf{E},$$

where we used the fact that the ∂_t operation is scalar (does not introduce ties between the positional dimensions) and therefore the order of operations can be swapped and Ampère-Maxwell's law. Putting these two results together gives the wave equation for \mathbf{E}

$$\nabla^2 \mathbf{E} - \varepsilon\mu_0 \partial_t^2 \mathbf{E} = 0. \quad (\square \mathbf{E})$$

An analogous sequence of operations leads to the wave equation for \mathbf{B}

$$\nabla^2 \mathbf{B} - \varepsilon\mu_0 \partial_t^2 \mathbf{B} = 0. \quad (\square \mathbf{B})$$

Comparing the general n -dimensional wave equation $(\square_v \Psi)$ with the wave equations $\square \mathbf{E}$ and $\square \mathbf{B}$, we can determine the propagation speed v of the EM wave in the medium as

$$\varepsilon\mu_0 = 1/v^2 \implies v = \frac{1}{\sqrt{\varepsilon\mu_0}}.\tag{1.2}$$

This is in accordance with the known value of the speed of light in vacuum $c = \frac{1}{\sqrt{\varepsilon_0\mu_0}} = 299\,792\,458$ m/s.

1.3 Solutions to the Wave Equation of Light

There are two solutions to Equation $\square_v \Psi$ that will be of interest to us. They differ by the shape of the wave-front surface that is produced.

[4]: Feynman et al. (2011), *Feynman Lectures on Physics, Vol. II: The New Millennium Edition: Mainly Electromagnetism and Matter*

First we have the *spherical wave*, that is more aligned with the apprehension of light sources in fluorescent microscopy (FM) in theory as will become apparent. There is a problem with the spherical wave solution that will be demonstrated, hence, the *planar wave* solution will be also derived.

Spherical Wave

Let us consider a solution Ψ to the 3-dimensional wave equation ($\square_v \Psi$) that is dependent only on the radial distance from the origin $r = \sqrt{x^2 + y^2 + z^2}$ and time t . The Laplace operator ∇^2 of Ψ gives us

$$\begin{aligned} \nabla^2 \Psi &= \sum_{i=1}^3 \frac{\partial^2 \Psi(r)}{\partial x_i^2} = \sum_{i=1}^3 \frac{\partial}{\partial x_i} \left(\frac{\partial \Psi(r)}{\partial x_i} \right) = \sum_{i=1}^3 \frac{\partial}{\partial x_i} \left(\frac{\partial \Psi(r)}{\partial r} \frac{\partial r}{\partial x_i} \right) \\ &= \sum_{i=1}^3 \frac{\partial}{\partial x_i} \left(\frac{\partial \Psi(r)}{\partial r} \frac{x_i}{r} \right) = \sum_{i=1}^3 \frac{x_i}{r} \frac{\partial^2 \Psi(r)}{\partial x_i \partial r} + \frac{\partial}{\partial x_i} \left(\frac{x_i}{r} \right) \frac{\partial \Psi(r)}{\partial r} \\ &= \sum_{i=1}^3 \left(\frac{x_i}{r} \right)^2 \frac{\partial^2 \Psi(r)}{\partial r^2} + \frac{1}{r} \left(1 - \frac{x_i^2}{r^2} \right) \frac{\partial \Psi(r)}{\partial r} = \frac{\partial^2 \Psi(r)}{\partial r^2} + \frac{2}{r} \frac{\partial \Psi(r)}{\partial r} \\ &= \frac{1}{r} \frac{\partial^2}{\partial r^2} (r \Psi(r)). \end{aligned}$$

If rewrite the wave equation with this result and expand both sides by r , we get

$$\begin{aligned} \frac{1}{r} \frac{\partial^2}{\partial r^2} (r \Psi) - \frac{1}{v^2} \frac{\partial^2 \Psi}{\partial t^2} &= 0, \\ \frac{\partial^2}{\partial r^2} (r \Psi) - \frac{1}{v^2} \frac{\partial^2 r \Psi}{\partial t^2} &= 0, \\ \nabla^2 (r \Psi) - \frac{1}{v^2} \frac{\partial^2 r \Psi}{\partial t^2} &= 0, \end{aligned}$$

which is the wave equation ($\square_v \Psi$) in one dimension for the function $r \Psi$. The solution to the one-dimensional wave equation is in the form the d'Alembert's solution

$$\tilde{\Psi}(r, t) = \phi_{\rightarrow}(r - vt) + \phi_{\leftarrow}(r + vt). \quad (\text{d'Alembert's solution})$$

Of the two solutions, only the outwards propagated component ϕ_{\rightarrow} makes physical sense for a point source generating the spherical wave, so in the standard result, ϕ_{\leftarrow} is omitted by setting it to a zero function $\phi_{\leftarrow} \equiv 0$. The final spherical solution Ψ_{\circ} for light at the point $\vec{r} = (x, y, z)$ is

$$\Psi_{\circ}(\vec{r}, t) = \frac{\phi_{\rightarrow}(|\vec{r}| - vt)}{|\vec{r}|}. \quad (1.3)$$

One consideration is left to be discussed about this solution before reinterpreting it for the EM field. As you may have noticed in this section, the notation of Ψ has been used instead of Ψ . Before pronouncing the solution as a EM field solution, it is imperative to verify the consistency of it with Maxwell's equations, because it is implied that the solution

to Maxwell's equations are also EM wave equation solutions, but the inverse is not true. In fact this solution is a counter example to the inverse implication, since due to Birkhoff's theorem, this solution is in conflict with source-free Maxwell's equations while assuming that the solution is *non-static*, which means $v \neq 0$ in the terms of the derived Ψ_0 . To see this, let us start with the ansatz of a spherically symmetric field

$$\begin{aligned}\mathbf{E}(\vec{r}, t) &= E(r, t)\hat{\mathbf{r}}, \\ \mathbf{B}(\vec{r}, t) &= B(r, t)\hat{\mathbf{r}},\end{aligned}$$

where $\hat{\mathbf{r}}$ is the unit vector in the direction of \vec{r} . Plugging this into the right sides of Faraday's and Ampère-Maxwell's equations gives

$$\begin{aligned}\nabla \times \mathbf{E} &= \nabla \times E(r, t)\hat{\mathbf{r}} = \vec{0}, \\ \nabla \times \mathbf{B} &= \nabla \times B(r, t)\hat{\mathbf{r}} = \vec{0},\end{aligned}$$

hence the left sides follow as

$$\begin{aligned}-\partial_t \mathbf{B} &= \vec{0}, \\ \varepsilon\mu_0 \partial_t \mathbf{E} &= \vec{0},\end{aligned}$$

so the field is necessarily static for non-zero ε and μ , which is the only physical possibility for these quantities. It may be argued that a static solution, is also a possible solution, but it must be realized, that a static field implies an energy flux of zero and therefore cannot be a manifestation of light since no energy is transmitted.

A thought that we went astray with this solutions derivation is wrong however. Even though the solution is non-physical, it is widely used in optics, especially in diffraction theory, as an approximation to the true physical solution to avoid analytical dead-ends in the calculations. To this purpose, in conclusion, the approximation of the \mathbf{E} component of the EM field solution is

$$E_o(\vec{r}, t) = \frac{F\left(|\vec{r}| - \frac{t}{\sqrt{\varepsilon\mu_0}}\right)}{|r|},$$

where $F := \phi_{\rightarrow}$ is a chosen function. An analogous expression is available for \mathbf{B} .

The interesting observation to be made is that the intensity of the EM field declines in an inverse proportion to the radial distance r from the source. This can be intuitively realized by considering the fact that the wave-front surface is growing in a quadratic relation with distance r and the energy transmitted by the wave is also in a quadratic relation to E . Since the medium is non-dispersive, energy is not lost during the transmission and $E^2 \cdot S_{\text{wave-front}} \propto 1(r)$.

As for the adequacy of the spherical solution compared to the planar wave solution, we can conceptualize the source of radiation in FM as an electron of a fluorescent molecule in an excited state falling to the ground state while releasing a photon of a particular wavelength. Due to the small size of an atom with the dimensionality in the order of 1 \AA relative to the dimensionality of the field quantities such as the

wavelength in the order of 100 nm, the source of the field may be imagined as a point source, which is consistent with the imagination of the source, causing a spherical wave [5].

[5]: Aguet (2009), *Super-Resolution Fluorescence Microscopy Based on Physical Models*

Planar Wave

For the development of a plane wave, we can benefit by starting with the solution to the one-dimensional wave (d'Alembert's solution). Let us define the unit vector $\hat{\mathbf{n}}$ of direction of propagation of the \mathbf{E} -wave ($|\hat{\mathbf{n}}| = 1$) and the *wave vector* $\vec{k} = k\hat{\mathbf{n}}$. Next let us rewrite Gauss's law for \mathbf{E} (Eq. (1.1)) in the orthogonal basis $(\hat{\mathbf{n}}, \hat{\mathbf{n}}_{\perp 1}, \hat{\mathbf{n}}_{\perp 2})$

$$\nabla \cdot \mathbf{E} = \partial_{\hat{\mathbf{n}}}(\mathbf{E})_{\hat{\mathbf{n}}} + \partial_{\hat{\mathbf{n}}_{\perp 1}}(\mathbf{E})_{\hat{\mathbf{n}}_{\perp 1}} + \partial_{\hat{\mathbf{n}}_{\perp 2}}(\mathbf{E})_{\hat{\mathbf{n}}_{\perp 2}} = 0, \quad (1.4)$$

where $\partial_{\hat{\mathbf{v}}}$ is the spatial partial derivative in the direction of $\hat{\mathbf{v}}$ and $(\mathbf{E})_{\hat{\mathbf{v}}}$ is the basis vector $\hat{\mathbf{v}}$ component of \mathbf{E} . The assumption that the wave is propagating in the direction $\hat{\mathbf{n}}$ implies

$$\begin{aligned} \partial_{\hat{\mathbf{n}}_{\perp 1}}(\mathbf{E})_{\hat{\mathbf{n}}_{\perp 1}} &= 0, \\ \partial_{\hat{\mathbf{n}}_{\perp 2}}(\mathbf{E})_{\hat{\mathbf{n}}_{\perp 2}} &= 0, \end{aligned}$$

which when plugged into Equation 1.4 in turn implies

$$\partial_{\hat{\mathbf{n}}}(\mathbf{E})_{\hat{\mathbf{n}}} = 0.$$

If we now consider Ampère-Maxwell's law of Equation 1.1 and again assume that the \mathbf{B} -wave is propagating in the direction of $\hat{\mathbf{n}}$, meaning

$$\begin{aligned} \partial_{\hat{\mathbf{n}}_{\perp 1}}(\mathbf{B})_{\hat{\mathbf{n}}_{\perp 1}} &= 0, \\ \partial_{\hat{\mathbf{n}}_{\perp 2}}(\mathbf{B})_{\hat{\mathbf{n}}_{\perp 2}} &= 0, \end{aligned}$$

and therefore

$$(\nabla \times \mathbf{B})_{\hat{\mathbf{n}}} = 0,$$

so we obtain that $(\mathbf{E})_{\hat{\mathbf{n}}}$ is constant in time. This implies, that is we assume a dynamic \mathbf{E} -field, $(\mathbf{E})_{\hat{\mathbf{n}}} \equiv 0$. To put this into words, we can say that for the propagation of planar waves in the direction $\hat{\mathbf{n}}$, \mathbf{E} is perpendicular to the direction of propagation, $\mathbf{E} \perp \hat{\mathbf{n}}$. Since we know that \mathbf{E} lies in the plane $\hat{\mathbf{n}}_{\perp 1} \times \hat{\mathbf{n}}_{\perp 2}$, we can denote the direction $\mathbf{E}/|\mathbf{E}| =: \hat{\mathbf{m}}$ and change reinterpret \mathbf{E} in the basis $(\hat{\mathbf{n}}, \hat{\mathbf{m}}, \hat{\mathbf{x}}_{\perp})$. The calculation of $\nabla \times \mathbf{E}$ is now trivial, as the only non-zero component of \mathbf{E} is $(\mathbf{E})_{\hat{\mathbf{m}}}$ and so

$$\begin{aligned} (\nabla \times \mathbf{E})_{\hat{\mathbf{n}}} &= (\nabla \times \mathbf{E})_{\hat{\mathbf{m}}} = 0, \\ (\nabla \times \mathbf{E})_{\hat{\mathbf{x}}_{\perp}} &= \partial_{\hat{\mathbf{n}}}(\mathbf{E})_{\hat{\mathbf{m}}}. \end{aligned}$$

Now we can see that if \mathbf{E} is in the direction of $\hat{\mathbf{m}}$ then substituting the curl of \mathbf{E} into Faraday's law (Eq. (1.1))

$$\begin{aligned} \partial_t(\mathbf{B})_{\hat{\mathbf{m}}} &= \partial_t(\mathbf{B})_{\hat{\mathbf{m}}} = 0, \\ \partial_t(\mathbf{B})_{\hat{\mathbf{x}}_{\perp}} &= \partial_{\hat{\mathbf{n}}}(\mathbf{E})_{\hat{\mathbf{m}}}, \end{aligned}$$

and we can again leverage the assumption of a dynamic \mathbf{B} -field and conclude that if the wave propagates in the direction $\hat{\mathbf{n}}$, then the direction of the \mathbf{E} -field is $\hat{\mathbf{m}}$ and the direction of the \mathbf{B} -field is the perpendicular $\hat{\mathbf{x}}_{\perp}$. In summary $\mathbf{E} \perp \mathbf{B} \perp \hat{\mathbf{n}}$. The same argument can be used to determine the curl $\nabla \times \mathbf{B}$ which results in the singular non-zero component

$$(\nabla \times \mathbf{B})_{\hat{\mathbf{m}}} = \partial_{\hat{\mathbf{n}}}(\mathbf{B})_{\hat{\mathbf{x}}_{\perp}} = \varepsilon\mu_0 \partial_t(\mathbf{E})_{\hat{\mathbf{m}}}.$$

We have arrived at two equations that tie the \mathbf{E} -field and \mathbf{B} -field together

$$\partial_t(\mathbf{B})_{\hat{\mathbf{x}}_{\perp}} = \partial_{\hat{\mathbf{n}}}(\mathbf{E})_{\hat{\mathbf{m}}}, \quad (1.5)$$

$$\partial_{\hat{\mathbf{n}}}(\mathbf{B})_{\hat{\mathbf{x}}_{\perp}} = \varepsilon\mu_0 \partial_t(\mathbf{E})_{\hat{\mathbf{m}}}. \quad (1.6)$$

To put this all together and finish the planar wave solution we only need to apply $\partial_{\hat{\mathbf{n}}}$ to Equation 1.5 and ∂_t to Equation 1.6 and observe that the right sides of both equations are identical implying the equality of the left sides

$$\partial_{\hat{\mathbf{n}}}^2(\mathbf{E})_{\hat{\mathbf{m}}} - \varepsilon\mu_0 \partial_t^2(\mathbf{E})_{\hat{\mathbf{m}}} = 0. \quad (1.7)$$

If we make the analogous last step for the \mathbf{B} -field, we get

$$\partial_{\hat{\mathbf{n}}}^2(\mathbf{B})_{\hat{\mathbf{x}}_{\perp}} - \varepsilon\mu_0 \partial_t^2(\mathbf{B})_{\hat{\mathbf{x}}_{\perp}} = 0. \quad (1.8)$$

Observing the equations Equation 1.7 and Equation 1.8, it is clear that they are one-dimensional wave equations and the d'Alembert's solution, can be used to specify the form of the fields

$$\begin{aligned} (\mathbf{E}(\vec{r}, t))_{\hat{\mathbf{m}}} &= \phi_{\rightarrow}^{\mathbf{E}}\left((\vec{r})_{\hat{\mathbf{n}}} - \frac{t}{\sqrt{\varepsilon\mu_0}}\right) + \phi_{\leftarrow}^{\mathbf{E}}\left((\vec{r})_{\hat{\mathbf{n}}} + \frac{t}{\sqrt{\varepsilon\mu_0}}\right) \\ (\mathbf{B}(\vec{r}, t))_{\hat{\mathbf{x}}_{\perp}} &= \phi_{\rightarrow}^{\mathbf{B}}\left((\vec{r})_{\hat{\mathbf{n}}} - \frac{t}{\sqrt{\varepsilon\mu_0}}\right) + \phi_{\leftarrow}^{\mathbf{B}}\left((\vec{r})_{\hat{\mathbf{n}}} + \frac{t}{\sqrt{\varepsilon\mu_0}}\right). \end{aligned}$$

Based on empirical physical properties of the wave, in contemporary physics, we omit ϕ_{\leftarrow} and are left with the retarded time solutions

$$(\mathbf{E}(\vec{r}, t))_{\hat{\mathbf{m}}} = \phi^{\mathbf{E}}\left((\vec{r})_{\hat{\mathbf{n}}} - \frac{t}{\sqrt{\varepsilon\mu_0}}\right), \quad (1.9)$$

$$(\mathbf{B}(\vec{r}, t))_{\hat{\mathbf{x}}_{\perp}} = \phi^{\mathbf{B}}\left((\vec{r})_{\hat{\mathbf{n}}} - \frac{t}{\sqrt{\varepsilon\mu_0}}\right). \quad (1.10)$$

To clean up the notation, we restore the standard Cartesian coordinate system as $(\hat{\mathbf{n}}, \hat{\mathbf{m}}, \hat{\mathbf{x}}_{\perp}) = (\hat{\mathbf{x}}, \hat{\mathbf{y}}, \hat{\mathbf{z}})$ and $\mathbf{E} = (E_x, E_y, E_z)$, $\mathbf{B} = (B_x, B_y, B_z)$ and denote the retarded x -coordinate $x - \frac{t}{\sqrt{\varepsilon\mu_0}}$ as ξ .

This is not the final result though, since we can determine the relation of $\phi^{\mathbf{E}}$ and $\phi^{\mathbf{B}}$ by using one of the established equations 1.5 and 1.6. We first substitute \mathbf{E} and \mathbf{B} into the equation 1.5 from equations 1.7 and 1.8

$$\partial_t \phi^{\mathbf{B}}(\xi) = \partial_x \phi^{\mathbf{E}}(\xi),$$

which evaluates to

$$-\frac{1}{\sqrt{\varepsilon\mu_0}} \frac{d\phi^{\mathbf{B}}}{d\xi} = \frac{d\phi^{\mathbf{E}}}{d\xi},$$

and so with the reminder that $\sqrt{\varepsilon\mu_0} = 1/v$, we can conclude that

$$\phi^{\mathbf{B}}(\xi) = -\frac{1}{v} \frac{d\phi^{\mathbf{E}}}{d\xi}, \quad (1.11)$$

where the constant additive coefficient was omitted similarly as before, because we are deriving only the dynamic relations and are not interested in the electro-static and magneto-static fields, since they are not bearers of energy.

Putting everything together using equations 1.9, 1.10 and 1.11, we get the EM plane wave

$$E_y(\vec{r}, t) = F\left(x - \frac{t}{\sqrt{\varepsilon\mu_0}}\right), \quad (1.12)$$

$$B_z(\vec{r}, t) = \frac{1}{\sqrt{\varepsilon\mu_0}} F\left(x - \frac{t}{\sqrt{\varepsilon\mu_0}}\right), \quad (1.13)$$

where $F := \phi_{\vec{x}}^{\mathbf{E}}$ is a chosen function.

A similar note must be made about the validity of this solution as in Subsection 1.3. Although it is a solution to Maxwell's equations (Eq. (1.1)) unlike the spherical wave, there is no physical source that can generate this exact solution. A possible non-physical source would be an infinite plane that changes its charge. We use this solution as an approximation, and a good one undeniably, which upholds the wave-front shape when the source is far from the assessed location (the far-field region) and the propagating wave-front can endure its strength as in the solution, if we are simultaneously far from the source and we assess the wave-front over a small distance relative to the distance of the source⁵.

5: This makes it the relevant solution, when it comes to astronomy, where the light comes from far distances and the relative size of the telescope is miniscule compared to them.

Harmonic Waves

Harmonic waves play a special role in the theory of EM field. This is due to the fact that Maxwell's equations are linear and therefore, any function F from subsections 1.3 and 1.3 that can be expressed in the form of harmonics can be expressed in the form of spherical and planar harmonic waves respectively.

A harmonic plane wave has the form

$$\begin{aligned} \mathbf{E}(\vec{r}, t) &= \vec{E}_0 e^{-j(\omega t - \vec{k} \cdot \vec{r})}, \\ \mathbf{B}(\vec{r}, t) &= \vec{B}_0 e^{-j(\omega t - \vec{k} \cdot \vec{r})}, \end{aligned} \quad (1.14)$$

where the vectors \vec{E}_0, \vec{B}_0 and \vec{k} form an orthogonal bases.

2

Super-resolution Microscopy

| | |
|------------------------------|----|
| 2.1 Comparison of SR | |
| Methods | 12 |
| 2.2 Principle of SIM | 15 |
| 2.3 SIM | 16 |
| 2.4 Discussion | 17 |

[6]: Cremer et al. (1978), *Considerations on a Laser-Scanning-Microscope with High Resolution and Depth of Eld*

An important fact that should be realized is that that mostly none of the SR methods described here are useful in other optical acquisition contexts then in microscopy. This is due to the property, that the methods rely on the ability to closely control the environment of the observation in various ways. As an example, SIM is impossible to mimic, within the context of astronomy because we can not vary the illumination and in fact do not observe reflections of or emission due to illuminating the field.

[7]: Guerra (1995), *Super-Resolution through Illumination by Diffraction-Born Evanescent Waves*

[8]: Heintzmann et al. (1999), *Laterally Modulated Excitation Microscopy: Improvement of Resolution by Using a Diffraction Grating*

[9]: Weiss (2014), *Nobel Prizes for Super-Resolution Imaging*

[10]: Lal et al. (2016), *Structured Illumination Microscopy Image Reconstruction Algorithm*

In the realm of optical microscopy, the pursuit of enhanced spatial resolution has led to the development of various techniques collectively known as SR microscopy. The central aspect to the term super-resolution is the ability to surpass the classical established diffraction resolution limit by means of the technique.

SR microscopy has been a term and a topic of study for almost half a century now. In 1978, the first method to be developed, that may be categorized as a SR method, is the so called $4\pi\text{M}$ by *Christoph and Thomas Cremer* [6]. It rethinks the classical design of sample illumination and attempts to limit the volume that is excited by the radiation within the sample space within one acquisition. The light in the image space is thus reduced to the emission of the fluorescent molecules within this volume of the sample and a reduction in uncertainty of the location within this volume of the sample is achieved. By the repetition of these localized acquisitions, it is then possible to systematically cover the sample space and reconstruct the full sample estimate based on information from all of the acquisitions. The realization that outperforming the classical diffraction limit by means of a specialized modality or setup of the microscope is possible resulted in a rapid pace of innovation and lead to the invention of novel techniques, altering the way of illuminating the sample and the preparation of the imaged sample itself.

A major breakthrough was presented in 1995 by *J. Guerra*, who made use of a non-physical method to achieve SR in theory by including a modulation of the transfer function into the acquisition process and evaluating the effect on the dependence of observed light in the image space on the source signal [7]. Later in 1999 *Heintzmann and Gustafsson* developed a deconvolution based reconstruction algorithm for *Guerra's* method [8]. This change in perspective was also met with a large number of follow-ups which explored further approaches of utilizing the concept transfer function manipulation and pre-transfer inferred response signal control for the purpose of achieving SR.

The culminated effort within the microscopy field lead to numerous advancements and unprecedented observations mostly in biology. As a result and a appreciation was the granting of the Nobel Prize in Chemistry in 2014 shared three scientists who developed the stimulated emission depletion (STED) method [9].

2.1 Comparison of SR Methods

To this date, there are two major broad approaches of achieving SR that have been demonstrated in practice [10]. In some modern cases a combination of methods one from each of the approach can be used

alongside each other for achieving a greater resolution than one that is achievable by using them in isolation. These broad categories are:

localization Concerns with reducing signal from the source structure to a limited volume or volumes that are sparse within the image plane. This bypasses the resolving limit using employing the aspect of the sensed signal, that there is assumed to be little superposition from the individual fluorescent molecules. Lack of superposition can be used to distinguish individual emitting particles and if enough photons from one such particle is collected, its position can be determined with a low uncertainty.

modulation By altering one of the aspect of generation of signal from the source structure, it induces a superposition of source signals caused by a range or discrete set of scales within the source structure. With a prior expectation or design of the set of scales superposed (aliased) and often by use of more than one such acquisition with different sets of scales admitted or included with a different factor within the superposition, the scales can be distinguished and mapped to the original scale of the source by reconstruction from the individual acquisitions.

Usually a *localization* based method uses illumination volume reduction for the purpose of limiting the volume of source structure originated signal in the sensed signal, it requires scanning or varying the location of the volume in a different manner in order to make a reconstruction of the full field source signal. This is often at the demise of temporal resolution or alternatively an acquisition prioritizing temporal speed can severely reduce the resolution gain in the space axes. In other words, fast localization SR acquisitions usually do not retain their advertised SR to the extent of still and long lasting acquisitions. Aforementioned is a substantial case for using *modulation* based methods for dynamic sources acquisitions.

The *modulation* approach is a good fit for a dynamic (video) acquisition, since the photon efficiency relative to the efficiency of a standard acquisition is not lowered by a significant amount. That is important due to the fact that if we want to acquire a live-cell for a period of time, it is desirable to limit the fluorophore bleaching caused by the cumulative effect of illumination during this time. A popular choice for live-cell acquisitions is therefore SIM.

A non-exhaustive table of SR methods is presented in Table 2.1.

| SR Method | Method Summary | Resolution | | | Year of Origin |
|---|--|------------|--------|----------|----------------|
| | | Lateral | Axial | Temporal | |
| FIONA [11] • widefield • localization | Labels the sample with a single fluorophore within a diffraction radius. Collects a sufficient number of photons from the isolated fluorophores to alleviate location noise and uses curve fitting to find the center of the diffraction pattern that is assumed to be the true fluorophore location. | 1.5 nm | N/A | 0.5 s | 2003 |
| STED [12] • scanning • localization | Uses two laser beams for illumination: an excitation beam and a STED beam. The excitation beam excites the fluorophore photons and therefore causes fluorescence in the sample, while the STED beam, focused with small lateral offsets, depletes fluorescence in the outer regions of the excitation spot reducing the volume where fluorophores are excited. | 25 nm | 100 nm | 5 ms | 1994 |
| PALM [13] • widefield • localization | Stimulates the fluorophore labels in the sample with light and switching them from between the states of emitting and bleached, which is a state due to over activation of the fluorophore that wears off with passing time. This is done in such a manner that the number of activated fluorophores is low and sparse within the sample. Similarly to FIONA, this ensures their precise localization. It enough cycles are performed for a each set of fluorophores, a full image can be obtained by stacking the source estimations from each stack. | 2 nm | 10 nm | 5 s | 2006 |
| STORM [14, 15] • widefield • localization | The idea is the same as in PALM. Unlike PALM, the sample is stained with specialized dyes that are photo-switchable. This means unlike PALM no reliance is placed on the time it takes for the fluorophores to revive from the bleached state and the switching may be done faster to the benefit of the temporal resolution. | 4 nm | 10 nm | 1 s | 2006 |
| 4 π M [6] • scanning • localization | Uses the two opposing objective lenses focused on the same location within the sample. Further more, it uses a laser that is via reflection directed from both sides precisely aligned in relation to the sample and the reflected and emitted light can be collected leading to the ability of detecting the depth of the fluorophores by the effect of assessing, where relative to the laser beam wavelength the emission happens with better resolution. It improves only the axial resolution (using a classical wide-field microscope it is about 500 nm). | 180 nm | 100 nm | 50 ms | 1978 |
| SIM [7, 8, 16] • widefield • modulation | An illumination with non-uniform (modulated) intensity is used with sub-diffraction resolution lateral variations. These variations modify the signal produced by the sample structure and shifts some of its variations that are too rapid for the diffraction-limit and would not "survive" the optical system into lesser ones. This leads to aliasing within the sensed signal. It is possible to determine and the original locations of the variations, by an acquisition of multiple modulations and a reconstruction can be performed. | 40 nm | 300 nm | 100 ms | 1995 |

Table 2.1: The most prolific SR methods and their approximate optimal resolutions achievable in each axis as of January 2024. Keep in mind that the resolutions listed are optimal and are not, and often can not, be achieved in one acquisition, because there is in most cases a compromise to be made. If the resolving power for a single axis is optimized, the others suffer a loss in attainable resolution. An extreme example of this is PALM, where the maximum frame rate is about 12 min^{-1} but an acquisition with the best lateral resolution of 2 nm can take up to 12 h. *Widefield* signifies that the acquisition of the full frame is performed in one take and *scanning* that the acquisition of the full frame requires the accumulation of acquisition of multiple patches of different volumes of the sample space. Besides the impressive resolutions that are achieved by the SR methods, it speaks volumes about their inventors that they came up with some of the cheekiest acronyms widely used in contemporary science of today.

2.2 Principle of SIM

The principle which SIM and other modulation based SR methods stand on will be demonstrated by harmonic SIM. Harmonic SIM alters the signal generated by the source structure via non-uniform illumination. The illumination intensity takes the form of a 2D harmonic function.

As a first step, let us consider, how a harmonic may affect aliasing of a signal in a one-dimensional example. Let us have a model source structure, i.e. what we want to estimate, to be

$$s(x) = \cos(\omega x).$$

Now, we want to imitate the illumination. We can set the "illumination" as a harmonic in analog to the 2D harmonic in SIM that we want to get the intuition for

$$i(x) = \cos(\alpha \cdot \omega x),$$

where α is a constant. If we want to imitate SIM $\alpha \approx 1$ but $\alpha \neq 1$. To imitate the optical system, due to its linearity, it is adequate to perform the transfer of the "illumination", we multiply the source structure by it

$$\begin{aligned} g(x) &= s(x) \cdot i(x) = \cos(\omega x) \cdot \cos(\alpha \omega x) \\ &= \cos\left(\left(\frac{\alpha+1}{2} - \frac{\alpha-1}{2}\right) \cdot \omega x\right) \cdot \cos\left(\left(\frac{\alpha+1}{2} + \frac{\alpha-1}{2}\right) \cdot \omega x\right) \\ &= \frac{\cos((1+\alpha) \cdot \omega x) + \cos((\alpha-1) \cdot \omega x)}{2} \end{aligned}$$

We can see from the above that some of the scales of variation of s^1 were approximately doubled ($\alpha \approx 1$) but some on the other hand are very close to 0. This is the idea behind SIM, where the variation that is lowered can now be observed.

Even better than observing the exact case of a 1D imitation of SIM is to observe a physical analog in acoustics, that is often observed in real life. If two harmonic acoustic waves with similar frequencies are superposed a *beat* pattern emerges. The real life use of this phenomenon is in sirens on an ambulance or on a police vehicle. If we listen to them closely, it is possible to distinguish the high frequency harmonics and the low frequency beat sound. A depiction of this phenomenon can be seen in Figure 2.2.

There is also an illustrative phenomenon that is commonplace in the real world of the above concept from 1D in the 2D of SIM. It is in the form of *moiré fringes* (or patterns). They are present when two high-frequency patterns are superposed. Examples of this in common use (Fig. 2.3) are:

- ▶ A news anchorman with a striped shirt on an old low-resolution television. The patterns that are superposed are the stripes on the shirt and the scan-lines of the television.
- ▶ A close-up photo of an LCD or LED screen monitor. The pattern are the pixels rows and columns of the camera and the monitor.

1: Here, variations are not in the literal sense of the mathematics definition but rather intuitive variations as can be seen in Figure 2.1. Later in the 2D case, we will do all the operations in Fourier space and the so called scales of variation will be frequencies for us and the notion will stand on a firmer basis.

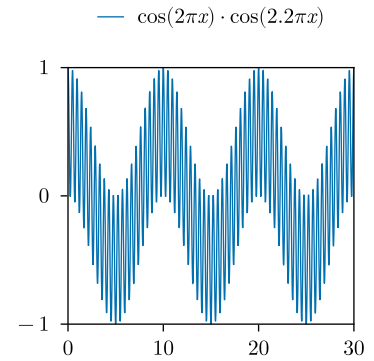


Figure 2.1: We can see how the multiplication with the "illumination" affects the signal g that is generated. Here, $\alpha = 1.1$. It is clear from the graph, what we intuitively mean by the variation.

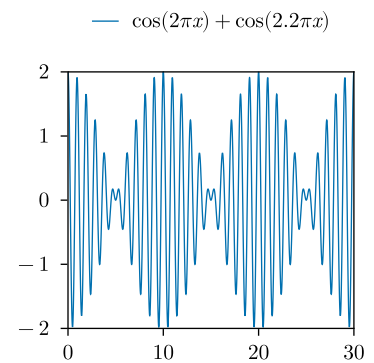


Figure 2.2: Acoustic beat pattern that emerges when two close frequency harmonics are superposed.

Scale of the patterns change when distance of the camera from the monitor.

- The citizenship ID card or a banknote, where moiré patterns are intentionally incorporated as a safety feature of the print.

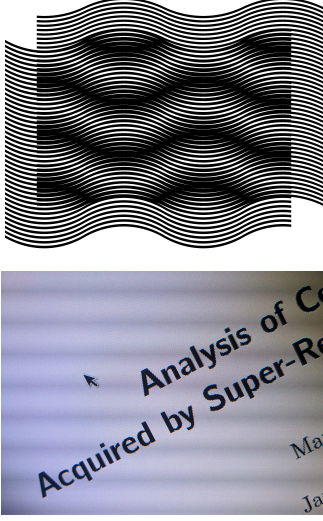


Figure 2.3: Moiré fringes are present when two high-frequency patterns are superposed.

(courtesy of Emin Gabrielyan)

2.3 SIM

The aliasing in harmonic SIM is better presented in the Fourier domain. We will denote the Fourier images of functions by capital letters. That is, we denote the Fourier image of the source s as $\mathcal{F}[s] = S$, the illumination i as $\mathcal{F}[i] = I$ and so on. This notation is also used in the experiment part.

The harmonic SIM illumination pattern as already mentioned is the harmonic cosine function. In 2D, this is

$$i_{(m, \vec{k}_i, \phi)}(\vec{r}) = 1 + \frac{m}{2} \cos(2\pi \vec{k}_i \cdot \vec{r} + \phi),$$

where m , \vec{k}_i and ϕ are constant parameters *modulation*, *phase-shift* (or *orientation*) and *phase-offset* of the illumination pattern respectively. The Fourier image of a 2D harmonic function is

$$\begin{aligned} \mathcal{F}[\cos(2\pi \vec{k}_i \cdot \vec{r})](\vec{k}) &= \frac{1}{2} \mathcal{F}[\exp(2\pi j \vec{k}_i \cdot \vec{r}) + \exp(-2\pi j \vec{k}_i \cdot \vec{r})](\vec{k}) \\ &= \frac{1}{2} \iint_{\mathbb{R}^2} (\exp(2\pi j \vec{k}_i \cdot \vec{r}) + \exp(-2\pi j \vec{k}_i \cdot \vec{r})) \\ &\quad \cdot \exp(-2\pi j \vec{k} \cdot \vec{r}) \, d\vec{r} \\ &= \frac{1}{2} \iint_{\mathbb{R}^2} \exp(2\pi j \vec{k}_i \cdot \vec{r}) \cdot \exp(-2\pi j \vec{k} \cdot \vec{r}) \, d\vec{r} \\ &\quad + \frac{1}{2} \iint_{\mathbb{R}^2} \exp(-2\pi j \vec{k}_i \cdot \vec{r}) \cdot \exp(-2\pi j \vec{k} \cdot \vec{r}) \, d\vec{r} \\ &= \frac{\mathcal{F}[\exp(2\pi j \vec{k}_i \cdot \vec{r})](\vec{k}) + \mathcal{F}[\exp(-2\pi j \vec{k}_i \cdot \vec{r})](\vec{k})}{2} \\ &= \frac{1}{2} \delta(\vec{k} + \vec{k}_i) + \frac{1}{2} \delta(\vec{k} - \vec{k}_i), \end{aligned}$$

which means that the Fourier image of the illumination pattern, due to linearity of \mathcal{F} is

$$\mathcal{F}[i_{(m, \vec{k}_i, \phi)}(\vec{r})](\vec{k}) = I_{(m, \vec{k}_i, \phi)}(\vec{k}) = \frac{m e^{-j\phi}}{4} \delta_{-\vec{k}_i} + \delta + \frac{m e^{j\phi}}{4} \delta_{+\vec{k}_i}.$$

We assume that the relation between excitation illumination intensity i and the emission intensity of a single fluorophore is linear. The relation between the emission intensity g at a point and the source structure s (i.e. the density of fluorescent particles) times the excitation intensity is also linear. In fact we assume that the multiplicative coefficient is 1 without loss in generality since we are not interested in the actual number of photons produced, but instead the structure variations and so, in the spatial domain

$$g(\vec{r}) = s(\vec{r}) \cdot i(\vec{r}).$$

We know that in the Fourier domain, this translates to the convolution, i.e.

$$G(\vec{k}) = S(\vec{k}) * I(\vec{k}).$$

From this, it is clear that the structured illumination of the sample, induces spatial frequency aliasing of the sample source s in the g signal. This signal is then propagated through the optical system via the transfer function to produce the sensed signal f . In the Fourier domain, this is expressed by

$$F(\vec{k}) = (S(\vec{k}) * I(\vec{k})) \cdot H(\vec{k}).$$

The reconstruction procedure then deals with antialiasing the frequencies of the sensed F and placing them into their correct locations within the reconstructed \hat{S} . From \hat{S} , we can then obtain the reconstructed spatial source as

$$\mathcal{F}^{-1}[\hat{S}] = \hat{s}.$$

This concept is further explained and performed in Chapter 3.

2.4 Discussion

Due to the fact that the only difference between the SIM based acquisition and a regular acquisition is the non-uniform illumination, SIM is composable with various setup modalities, available for regular view-field microscopy. For example, it can be used in combination with total internal reflection fluorescence microscopy (TIRFM), where noise can be reduced by reducing the illumination of the sample to a narrow axial slice. The data that we are working with in the later chapters is acquired with this modality.

We are also not limited to the case of harmonic illumination. There have been successful SIM demonstrations with apriori unknown speckle patterns, with only the singular condition, of summing into a uniform intensity [17, 18].

It is also not limited to lateral resolution enhancement. The harmonic patterns that we are using can also be expressed for axial slices that are not in one the focal plane and the 3D optical transfer function (OTF) can be used in the reconstruction to enhance the image resolution in both axial and lateral directions [16]. This approach requires 15 acquisitions with different parameters to in the reconstruction compared with 9 frame acquisitions of the standard Wiener filter based reconstruction for lateral resolution gain.

We are also not limited to a mere resolution doubling, as can be observed from Table 2.1 [19]. It is essential though to realize that the harmonic illumination pattern is limited in the intensity variation frequency similarly by diffraction similarly to the wide way the optical system limits the resolution by diffraction². This problem is overcome by utilization of the non-linearity of the relation between excitation and emission near the saturation point of the fluorophores. A non-linearity in the generation of photons by the fluorophores can be modelled and is desirable in this case, because it enables us to induce higher

[17]: Yeh et al. (2017), *Structured Illumination Microscopy with Unknown Patterns and a Statistical Prior*

[18]: Mudry et al. (2012), *Structured Illumination Microscopy Using Unknown Speckle Patterns*

[16]: Gustafsson et al. (2008), *Three-Dimensional Resolution Doubling in Wide-Field Fluorescence Microscopy by Structured Illumination*

[19]: Gustafsson (2005), *Nonlinear Structured-Illumination Microscopy: Wide-field Fluorescence Imaging with Theoretically Unlimited Resolution*

2: Thus $\alpha \approx 1$ in Section 2.2 is not only the best option from the resolution gain standpoint, but also a forced necessity in the SIM realization.

frequencies. Let $I_{\text{em}} = I_{\text{em}}(I_{\text{ex}})$ be the known non-linear relationship, where I_{em} is the emission intensity and I_{ex} is the excitation intensity. If we have the modulation m of I_{ex} , such that the peak intensities of I_{ex} are above the saturation point of the fluorophores, we can express the relation $I_{\text{em}}(I_{\text{ex}}(\vec{r}))$ by the sum of its harmonic components at a Fourier series. The frequency components of the source s corresponding to the Fourier series components of $I_{\text{em}}(I_{\text{ex}}(\vec{r}))$, including the higher frequencies than the ones included in the regular SIM, are aliased in the sensed image F . By multiple acquisitions and by using the calculated Fourier series coefficients, a chosen number of components can be linearly separated similarly as in Chapter 3, and the reconstruction \hat{S} can be assembled from these components. If you think about the aforementioned procedure, the lateral resolution that can be achieved is theoretically unlimited. What is the problem³? If we were to expand the relation $I_{\text{em}}(I_{\text{ex}}(\vec{r}))$ into its Fourier series, we would observe that the higher of the harmonic component $\zeta_k(\vec{r})$ the lower the corresponding coefficient ρ_k and at some point, the component would become undistinguishable from the photon noise. This approach has also been implemented in combination with the photo-switchable dyes from STORM, which achieved the lateral resolution of 50 nm [20].

3: There must be one, because the prospect of unlimited resolution is unthinkable.

[20]: Rego et al. (2012), *Nonlinear Structured-Illumination Microscopy with a Photoswitchable Protein Reveals Cellular Structures at 50-Nm Resolution*

EXPERIMENT

3 SIM Reconstruction

| | |
|--|-----------|
| 3.1 Parameter Estimation | 21 |
| Phase-shift Estimate | 22 |
| Phase-Offset and Modulation Estimate | 24 |
| 3.2 Wiener filter Reconstruction | 24 |
| Separation of Components (i.) | 25 |
| Shifting Components (ii. and iii.) | 25 |
| Wiener Filter (iv.) | 27 |
| Apodization | 28 |
| 3.3 Inversion Reconstruction | 29 |
| Forward Model | 29 |
| Loss Function | 30 |
| Regularization Term | 31 |
| Optimization | 31 |
| 3.4 Discussion | 32 |

1: In the following text, sensed images (i.e. signal that we measure at the sensor) will be called a low-resolution (LR) image and the reconstructed image will be called a high-resolution (HR) image. It is important to remember throughout the text that when talking about the sampled (discrete) LR image, it has different pixel dimensions (sampling rate) from the HR image.

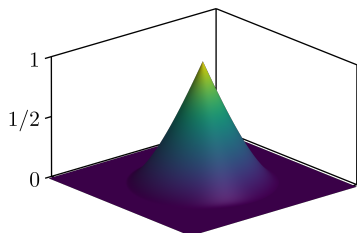


Figure 3.1: The OTF model of the optical system.

It was laid-out in the theory part, how to achieve introducing higher frequencies in the output image, which would be otherwise lacking in the regular wide-field microscope acquisition outputs. The process of reconstruction concerns with

- i. determining the powers of these aliased frequencies and
- ii. mapping their positions so that they are at the correct corresponding locations in the reconstructed image.

If everything is done correctly, it is possible to recover all the additional information from the newly introduced frequencies in the estimate of the source signal.

There is a multitude of approaches for performing these tasks, each of which has its own benefits and drawbacks. It is possible to categorise them into three broad categories based on the underlining theory that is used, namely:

- (a) Wiener filter based,
- (b) inversion/optimization based and
- (c) machine learning based.

At the input of our reconstruction are 9 LR¹ images acquired with 3 orientations (phase-shifts) that are spaced by approximately $2\pi/3$ to maximize information gain in the reconstructed image and every orientation is acquired with 3 phase-offsets (Fig. 3.2). The acquisition is made in an orientation-major fashion, meaning that all LR images of the same orientation are sensed before changing to the next orientation.

For most methods from the first two categories it is necessary to estimate some or all of the illumination pattern parameters of the LR images prior to the reconstruction. There again are many possible estimation algorithms relying on various assumptions, which are beneficial for acquisitions with specific properties, importantly differing in their robustness to noise contained in the LR images.

First, one such estimation sequence for determining the parameters, that has been tested to work well for the data we are working with, will be described (Sec. 3.1). The following sections will demonstrate the Wiener filter based approach (Sec. 3.2) and then the inversion/optimization based approach (Sec. 3.3). Lastly, some of the limitations and benefits of all three approaches will be discussed.

In this chapter, we will be using a model OTF (Fig. 3.1) supplied by the assembler of the microscope. It is derived from the ideal circular aperture OTF model with a curvature degradation of $\alpha = 0.9$. The formula for the OTF is

$$H(\vec{k}) = \frac{2}{\pi} \left(\arccos\left(\frac{|\vec{k}|}{2k_0}\right) - \frac{|\vec{k}|}{2k_0} \sqrt{1 - \frac{|\vec{k}|^2}{4k_0^2}} \right) \cdot \alpha^{|\vec{k}|/2k_0},$$

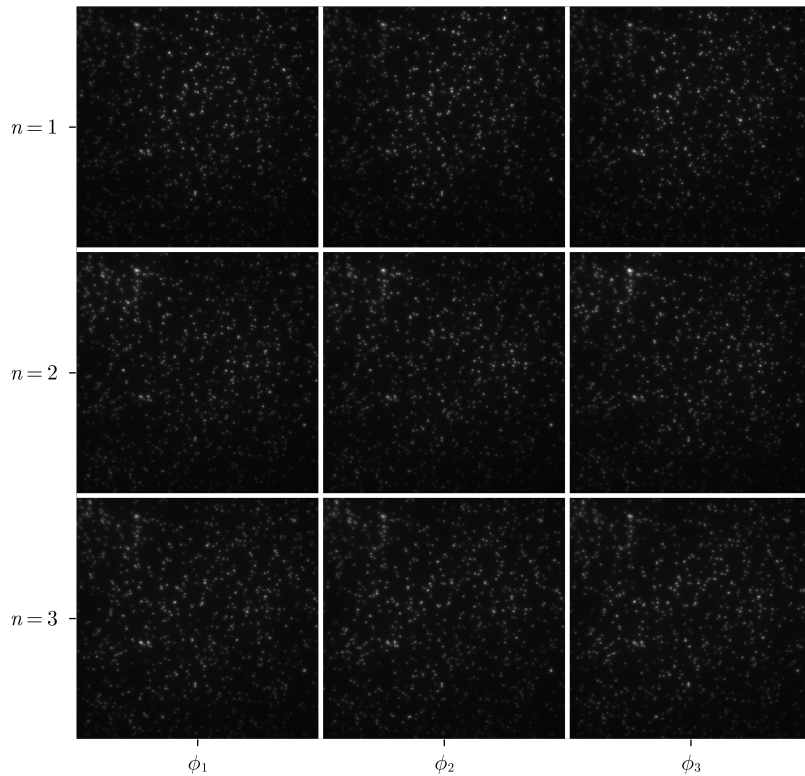


Figure 3.2: Acquisitions of 9 wide field images with harmonic patterned illuminations. The orientations are labelled $n = 1, 2, 3$ and the phases $\phi_i = \phi_1, \phi_2, \phi_3$. The order of acquisition is row-major in this figure.

where k_0 is the cut-off frequency of the OTF and for ρ the pupil radius the emission wavelength $\lambda_{\text{em}} = 488 \text{ nm}$, the distance between the entrance pupil and the focal plane f_R and the numerical aperture of the objective NA is

$$k_0 = \frac{\rho}{\lambda_{\text{em}} \cdot f_R} = \frac{2 \text{ NA}}{\lambda_{\text{em}}}.$$

3.1 Parameter Estimation

The general form of the LR image illumination patterns in one orientation, denoted i_{ϕ_1} , i_{ϕ_2} and i_{ϕ_3} , that are at the input of the Wiener filter reconstruction is

$$i_{\phi}(\vec{r}) = 1 + \frac{m}{2} \cos(2\pi \vec{k}_i \cdot \vec{r} + \phi), \quad (3.1)$$

where the phases $\phi_1 \neq \phi_2 \neq \phi_3$ and \vec{k}_i is the wave vector of the illumination pattern. An assumption that is made in our acquisition is that the phases differ by $2\pi/3$, that is

$$\phi_0 := \phi_1 = \phi_2 - 2\pi/3 = \phi_3 - 4\pi/3.$$

This assumption is based on the method that is employed for the generation of the illumination patterns, which should approximately guarantee this. Equivalently, due to the 2π period of the $\cos(x)$ function

in Equation 3.1, we adopt the notation

$$\begin{aligned} i_{\phi_1} &= i_{\phi_0} =: i_0, \\ \phi_- &:= \phi_0 - 2\pi/3 \quad \& \quad i_{\phi_3} = i_{\phi_-} =: i_-, \\ \phi_+ &:= \phi_0 + 2\pi/3 \quad \& \quad i_{\phi_2} = i_{\phi_+} =: i_+. \end{aligned}$$

As was demonstrated in the theory part, the acquisition carried out with an illumination pattern i_ϕ leads to the sensed LR image in the Fourier domain $F_\phi := \mathcal{F}[f_\phi]$ being

$$\begin{aligned} F_\phi &= \mathcal{F}[i_\phi \cdot s] \cdot H + N = (I_\phi * S) \cdot H + N \\ &= \underbrace{\left(\frac{me^{-i\phi}}{4} \delta_{-\vec{k}_i} + \delta + \frac{me^{i\phi}}{4} \delta_{+\vec{k}_i} \right)}_{I_\phi} * S \cdot H + N, \end{aligned} \quad (3.2)$$

where s/S is the source signal (i.e. the true structure), H is the OTF of the imaging system and N is noise in the Fourier domain. It can be observed from Equation 3.2, that the sensed LR image contains 3 bands (components) of aliased signal frequencies with frequency shifts of $-\vec{k}_i$, $\vec{0}$ and $+\vec{k}_i$. We can write the three acquisitions in one orientation as

$$\begin{pmatrix} F_{\phi_-} \\ F_{\phi_0} \\ F_{\phi_+} \end{pmatrix} = \begin{pmatrix} e^{\frac{+2\pi i}{3}} & 1 & e^{-\frac{2\pi i}{3}} \\ 1 & 1 & 1 \\ e^{-\frac{2\pi i}{3}} & 1 & e^{\frac{+2\pi i}{3}} \end{pmatrix} \begin{pmatrix} \frac{m}{4} e^{-i\phi_0} \cdot C_{-\vec{k}_i} \\ C_{\vec{0}} \\ \frac{m}{4} e^{+i\phi_0} \cdot C_{+\vec{k}_i} \end{pmatrix} + \begin{pmatrix} N_{\phi_-} \\ N_{\phi_0} \\ N_{\phi_+} \end{pmatrix}, \quad (3.3)$$

with the notation

$$\begin{pmatrix} C_{-\vec{k}_i} \\ C_{\vec{0}} \\ C_{+\vec{k}_i} \end{pmatrix}(\vec{k}) := H(\vec{k}) \begin{pmatrix} \delta_{-\vec{k}_i} * S \\ S \\ \delta_{+\vec{k}_i} * S \end{pmatrix}(\vec{k}) = H(\vec{k}) \begin{pmatrix} S(\vec{k} + \vec{k}_i) \\ S(\vec{k}) \\ S(\vec{k} - \vec{k}_i) \end{pmatrix}. \quad (3.4)$$

Phase-shift Estimate

First of the parameters that must be estimated is the phase-shift (i.e. wave vector of the illumination pattern) \vec{k}_i . First a separation of the shifted bands is performed while keeping the multiplicative coefficients² $\frac{m}{4} e^{-i\phi_0}$ and $\frac{m}{4} e^{+i\phi_0}$. This can be done by solving the linear system in Equation 3.3 for

$$\begin{pmatrix} \tilde{C}_{-\vec{k}_i} \\ C_{\vec{0}} \\ \tilde{C}_{+\vec{k}_i} \end{pmatrix} := \begin{pmatrix} \frac{m}{4} e^{-i\phi_0} \cdot C_{-\vec{k}_i} \\ C_{\vec{0}} \\ \frac{m}{4} e^{+i\phi_0} \cdot C_{+\vec{k}_i} \end{pmatrix}, \quad (3.5)$$

with disregard for noise. For the invertible symmetric matrix

$$\tilde{M} := \begin{pmatrix} e^{\frac{+2\pi i}{3}} & 1 & e^{-\frac{2\pi i}{3}} \\ 1 & 1 & 1 \\ e^{-\frac{2\pi i}{3}} & 1 & e^{\frac{+2\pi i}{3}} \end{pmatrix},$$

2: The reference phase-offset ϕ_0 is yet to be determined.

it is best to find \tilde{M}^{-1} using Cramer's rule, since many of the minors turn out to be equivalent

$$\begin{aligned}\tilde{M}^{-1} &= \begin{pmatrix} \begin{vmatrix} \tilde{M}_{22} & \tilde{M}_{23} \\ \tilde{M}_{32} & \tilde{M}_{33} \end{vmatrix} & -\begin{vmatrix} \tilde{M}_{21} & \tilde{M}_{23} \\ \tilde{M}_{31} & \tilde{M}_{33} \end{vmatrix} & \begin{vmatrix} \tilde{M}_{21} & \tilde{M}_{22} \\ \tilde{M}_{31} & \tilde{M}_{32} \end{vmatrix} \\ -\begin{vmatrix} \tilde{M}_{12} & \tilde{M}_{13} \\ \tilde{M}_{32} & \tilde{M}_{33} \end{vmatrix} & \begin{vmatrix} \tilde{M}_{11} & \tilde{M}_{13} \\ \tilde{M}_{31} & \tilde{M}_{33} \end{vmatrix} & -\begin{vmatrix} \tilde{M}_{11} & \tilde{M}_{12} \\ \tilde{M}_{31} & \tilde{M}_{32} \end{vmatrix} \\ \begin{vmatrix} \tilde{M}_{12} & \tilde{M}_{13} \\ \tilde{M}_{22} & \tilde{M}_{23} \end{vmatrix} & -\begin{vmatrix} \tilde{M}_{11} & \tilde{M}_{13} \\ \tilde{M}_{21} & \tilde{M}_{23} \end{vmatrix} & \begin{vmatrix} \tilde{M}_{11} & \tilde{M}_{12} \\ \tilde{M}_{21} & \tilde{M}_{22} \end{vmatrix} \end{pmatrix}^T \cdot \frac{1}{|\tilde{M}|} \\ &= \begin{pmatrix} e^{\frac{+2\pi i}{3}} & -2 \sin\left(\frac{+2\pi}{3}\right) & -e^{\frac{-2\pi i}{3}} \\ e^{\frac{+2\pi i}{3}} & 2 \sin\left(\frac{+2\pi}{3}\right) & e^{\frac{+2\pi i}{3}} \\ -e^{\frac{-2\pi i}{3}} & -2 \sin\left(\frac{+2\pi}{3}\right) & e^{\frac{+2\pi i}{3}} \end{pmatrix}^T \cdot \frac{1}{6 \sin\left(\frac{-2\pi i}{3}\right)} \\ &= \begin{pmatrix} \frac{-1}{4\sqrt{3}} + \frac{i}{4} & \frac{-1}{4\sqrt{3}} + \frac{i}{4} & \frac{-1}{4\sqrt{3}} - \frac{i}{4} \\ -\frac{1}{2} & \frac{1}{2} & -\frac{1}{2} \\ \frac{-1}{4\sqrt{3}} - \frac{i}{4} & \frac{-1}{4\sqrt{3}} + \frac{i}{4} & \frac{-1}{4\sqrt{3}} + \frac{i}{4} \end{pmatrix}.\end{aligned}$$

Finally, we have

$$\begin{pmatrix} \tilde{C}_{-\vec{k}_i} \\ C_{\vec{0}} \\ \tilde{C}_{+\vec{k}_i} \end{pmatrix}(\vec{k}) \approx \tilde{M}^{-1} \cdot \begin{pmatrix} F_{\phi_-} \\ F_{\phi_0} \\ F_{\phi_+} \end{pmatrix}(\vec{k}). \quad (3.6)$$

It is assumed that there is some overlap of the components $C_{\vec{0}}$ with both $C_{-\vec{k}_i}$ and $C_{+\vec{k}_i}$ within the support of the OTF³. Accordingly, estimate of \vec{k}_i is performed using cross-correlation [21]

$$\begin{aligned}\mathcal{C}_{+\vec{k}_i}(\vec{p}) &= \sum_{\vec{k}} \left(H(\vec{k} + \vec{p}) C_{\vec{0}}(\vec{k}) \right) \cdot \left(H(\vec{k}) \tilde{C}_{+\vec{k}_i}(\vec{k} + \vec{p}) \right) \\ &= \frac{m}{4} e^{+\phi_0} \sum_{\vec{k}} H(\vec{k} + \vec{p}) H(\vec{k}) S(\vec{k}) \\ &\quad \cdot H(\vec{k}) H(\vec{k} + \vec{p}) S(\vec{k} - \vec{k}_i + \vec{p}) \\ &= \frac{m}{4} e^{+\phi_0} \sum_{\vec{k}} H^2(\vec{k} + \vec{p}) H^2(\vec{k}) S(\vec{k}) S(\vec{k} - \vec{k}_i + \vec{p}).\end{aligned}$$

To make the estimate more robust to noise, we can instead use both components in the cross-correlation

$$\begin{aligned}\mathcal{C}(\vec{p}) &= \sum_{\vec{k}} \left(H(\vec{k} + \vec{p}) C_{\vec{0}}(\vec{k}) \right) \cdot \left(H(\vec{k}) \tilde{C}_{+\vec{k}_i}(\vec{k} + \vec{p}) \right) \\ &\quad + \sum_{\vec{k}} \left(H(\vec{k} - \vec{p}) C_{\vec{0}}(\vec{k}) \right) \cdot \left(H(\vec{k}) \tilde{C}_{-\vec{k}_i}(\vec{k} - \vec{p}) \right).\end{aligned} \quad (3.7)$$

We see from Equation 3.7 that \mathcal{C} is maximized, when the source signal arguments match,

$$S(\vec{k}) = S(\vec{k} - \vec{k}_i + \vec{p}) \implies \vec{k}_i = \vec{p},$$

and consequently the estimate can be made by maximizing the cross-

3: Unfortunately, there is an inverse relationship between how large the overlapping area is (therefore how robust the estimation is against noise) and the maximum achievable resolution, because, the larger the norm of \vec{k}_i is, the higher the maximum aliased frequency of the component, but the lower the overlap with the central component $C_{\vec{0}}$. Ultimately, most acquisitions using a shift estimation based on the cross-correlation make a compromise of these two effects and the phase-shift is placed approximately at 0.95 of the OTF cut-off frequency.

[21]: Huang et al. (2018), *Fast, Long-Term, Super-Resolution Imaging with Hessian Structured Illumination Microscopy*

correlation over values of \vec{p}

$$\hat{k}_i = \arg \max_{\vec{p}} \mathcal{C}(\vec{p}). \quad (3.8)$$

In practice, we cannot evaluate the functions $C_{-\vec{k}_i}(\vec{k})$ and $C_{+\vec{k}_i}(\vec{k})$ directly for an arbitrary value of $\vec{q} = \vec{k} + \vec{p} / \vec{q} = \vec{k} - \vec{p}$, since they are computed from the sampled, LR images. The solution to this is to evaluate them for the closest sampled frequency⁴ $[\vec{q}]$ and performing a shift by $(\vec{q} - [\vec{q}])$ using the Fourier shift theorem.

4: The closest reciprocal of a multiple of the LR image sampling step (i.e. pixel size).

Phase-Offset and Modulation Estimate

If we expand the components $\tilde{C}_{-\vec{k}_i}$ and $C_{\vec{0}}$ using Equation 3.3 and Equation 3.5 we get

$$\begin{aligned} \tilde{C}_{-\vec{k}_i}(\vec{k}) &= \frac{me^{-i\phi_0}}{4} C_{-\vec{k}_i} = \frac{me^{-i\phi_0}}{4} H(\vec{k}) S(\vec{k} + \vec{k}_i), \\ C_{\vec{0}}(\vec{k}) &= H(\vec{k}) S(\vec{k}). \end{aligned}$$

We see that they differ only by the phase-shift \vec{k}_i and the complex coefficient $me^{-i\phi_0}/4$. Using the phase-shift estimate $\hat{k}_i =: \vec{k}_i$, estimates of the source signal $S(\vec{k})$ and can be made from both components

$$\begin{aligned} \tilde{S}_{-\vec{k}_i}(\vec{k}) &= \frac{me^{-i\phi_0}}{4} \hat{S}_{-\vec{k}_i}(\vec{k}) = \frac{me^{-i\phi_0}}{4} \left(\frac{\tilde{C}_{-\vec{k}_i}(\vec{k} - \vec{k}_i)}{H(\vec{k} - \vec{k}_i)} \right), \\ \hat{S}_{\vec{0}}(\vec{k}) &= \frac{C_{\vec{0}}(\vec{k})}{H(\vec{k})}. \end{aligned}$$

Using complex linear regression from values in the intersection of $\text{supp } H(\vec{k} - \vec{k}_i)$ and $\text{supp } H(\vec{k})$, it is then possible to estimate $\tilde{m}/4 := me^{-i\phi_0}/4$ as

$$\begin{aligned} \Omega &= \text{supp } H(\vec{k} - \vec{k}_i) \cap \text{supp } H(\vec{k}) \\ \hat{m} &= \frac{4 \cdot \sum_{\vec{k} \in \Omega} \left(\tilde{S}_{-\vec{k}_i}(\vec{k}) \right)^* \cdot \hat{S}_{\vec{0}}(\vec{k})}{\sum_{\vec{k} \in \Omega} \hat{S}_{\vec{0}}^2(\vec{k})}. \end{aligned}$$

The modulation factor and the phase-offset estimates are consequently

$$\hat{m} = |\hat{m}| \quad \& \quad \hat{\phi}_0 = \arg(\hat{m}).$$

3.2 Wiener filter Reconstruction

The Wiener filter approach consists of:

- i. separation of the aliased components

$$\left(F_{\phi_-^n}^n, F_{\phi_0^n}^n, F_{\phi_+^n}^n \right)_{n \in [3]} \mapsto \left(C_{-\vec{k}_i}^n, C_{\vec{0}}^n, C_{+\vec{k}_i}^n \right)_{n \in [3]}$$

- ii. shifting the components to their corresponding locations within the HR image⁵

$$\left(C_{-\vec{k}_i}^n, C_{\vec{0}}^n, C_{+\vec{k}_i}^n \right)_{n \in [3]} \mapsto \left(C_{-\vec{k}_i}^{n'}, C_{\vec{0}}^{n'}, C_{+\vec{k}_i}^{n'} \right)_{n \in [3]}$$

- iii. determining the OTF of the mapped components and the HR image

$$\left(C_{-\vec{k}_i}^{n'}, C_{\vec{0}}^{n'}, C_{+\vec{k}_i}^{n'} \right)_{n \in [3]} \mapsto \left(H_{-\vec{k}_i}^{n'}, H_{\vec{0}}^{n'}, H_{+\vec{k}_i}^{n'} \right)_{n \in [3]}$$

- iv. application of the Wiener filter to the mapped components

$$\left(C_{-\vec{k}_i}^{n'}, C_{\vec{0}}^{n'}, C_{+\vec{k}_i}^{n'} \right)_{n \in [3]}, \left(H_{-\vec{k}_i}^{n'}, H_{\vec{0}}^{n'}, H_{+\vec{k}_i}^{n'} \right)_{n \in [3]} \mapsto \hat{S}.$$

Separation of Components (i.)

The procedure for Item i. was already described in Subsection 3.1. At this moment, however, we have the estimates of the phase-offsets ϕ_-, ϕ_0, ϕ_+ and the modulations m , therefore, we use them to separate the weighted components $C_{-\vec{k}_i}$, $C_{\vec{0}}$ and $C_{+\vec{k}_i}$. The linear combination matrix is now

$$\begin{aligned} M(m, \phi_0) &= \begin{pmatrix} \frac{m}{4} e^{\frac{+2\pi i}{3} - i\phi_0} & 1 & \frac{m}{4} e^{\frac{-2\pi i}{3} + i\phi_0} \\ \frac{m}{4} e^{-i\phi_0} & 1 & \frac{m}{4} e^{+i\phi_0} \\ \frac{m}{4} e^{\frac{-2\pi i}{3} - i\phi_0} & 1 & \frac{m}{4} e^{\frac{+2\pi i}{3} + i\phi_0} \end{pmatrix} \\ &= \tilde{M} \cdot \begin{pmatrix} \frac{me^{-i\phi_0}}{4} & \cdot & \cdot \\ \cdot & 1 & \cdot \\ \cdot & \cdot & \frac{me^{+i\phi_0}}{4} \end{pmatrix}, \end{aligned}$$

and M^{-1} is

$$\begin{aligned} M^{-1}(m, \phi_0) &= \begin{pmatrix} \frac{4e^{+i\phi_0}}{m} & \cdot & \cdot \\ \cdot & 1 & \cdot \\ \cdot & \cdot & \frac{4e^{-i\phi_0}}{m} \end{pmatrix} \cdot \tilde{M}^{-1} \\ &= \begin{pmatrix} \left(\frac{-1}{\sqrt{3}} + i \right) \cdot \frac{e^{+i\phi_0}}{m} & \frac{-1}{4\sqrt{3}} + \frac{i}{4} & \left(\frac{-1}{\sqrt{3}} - i \right) \cdot \frac{e^{-i\phi_0}}{m} \\ -\frac{2e^{+i\phi_0}}{m} & \frac{1}{2} & -\frac{2e^{-i\phi_0}}{m} \\ \left(\frac{-1}{\sqrt{3}} - i \right) \cdot \frac{e^{+i\phi_0}}{m} & \frac{-1}{4\sqrt{3}} + \frac{i}{4} & \left(\frac{-1}{\sqrt{3}} + i \right) \cdot \frac{e^{-i\phi_0}}{m} \end{pmatrix}. \end{aligned} \quad (3.9)$$

For every orientation $n \in [3]$ the separated components are

$$\begin{pmatrix} C_{-\vec{k}_i}^n \\ C_{\vec{0}}^n \\ C_{+\vec{k}_i}^n \end{pmatrix}(\vec{k}) \approx M^{-1}(m^n, \phi_0^n) \cdot \begin{pmatrix} F_{\phi_-^n}^n \\ F_{\phi_0^n}^n \\ F_{\phi_+^n}^n \end{pmatrix}(\vec{k}).$$

Shifting Components (ii. and iii.)

It is necessary need to shift the components to their locations corresponding to their location within the source signal. For a component $C_{\vec{p}}$ which corresponds to the element of the $I_{\vec{p}}$ with $\delta_{\vec{p}}$ we want to

5: In practice the components, when shifted, are placed within the HR image's grid (in the Fourier domain). We are working with a sensor that samples 512×512 pixels so these are the dimensions of the LR sensed images that are due to the imaging equipment. The dimensions of the output HR images are not predetermined or restricted by any external constraints and instead are a choice that is necessary to make. There is no reason to make the dimensions unnecessarily high since the amount of information in the reconstructed image is constant for any choice that is greater than the Shannon sampling rate of the reconstructed $\hat{s}(\vec{r})$. Assuming that the LR images are already sensed with a sampling rate above the Shannon threshold, we can set the HR image sampling rate to twice that of the LR images since the maximum theoretical enhancement in physical resolution (encapsulated information gain) for a reconstruction with linear SIM is $2\times$. With this in mind, the target dimensions of the reconstruction that we use is 1024×1024 .

The necessity of the separation of components is one of the major drawbacks for the Wiener filter approach, since it requires the acquisition of 9 LR images. We used all of the 9 LR images for the parameter estimation (Sec. 3.1), but if the parameters were known as a consequence to the method of acquisition, or they were estimated using a lower number of LR images, it wouldn't be possible to perform the reconstruction using the Wiener filter approach. It would however be possible to use the other two methods.

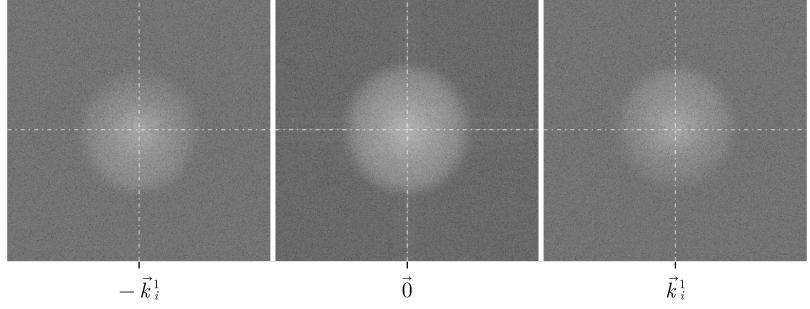


Figure 3.3: Separated components for orientation $n = 1$.

get $C'_{\vec{p}}(\vec{k}) = C_{\vec{p}}(\vec{k} + \vec{p})$. This is done using the Fourier shift theorem as

$$C'_{\vec{p}}(\vec{k}) = \mathcal{F}[\mathcal{F}^{-1}[C_{\vec{p}}](\vec{r}) \cdot e^{-2\pi i \vec{p} \cdot \vec{r}}](\vec{k}).$$

In this way, the shifting in Item ii. is performed for every component $C_{-\vec{k}_i^n}$, $C_{\vec{0}}$ and $C_{+\vec{k}_i^n}$ and for every orientation $n \in [3]$ (Fig. 3.4).

It is necessary to realize, how the frequencies in component $C'_{\vec{p}}$ manifest themselves in the sensed LR images F . The whole point of illuminating the image in a way that shifts the components towards lower frequencies is, that it moves them within the support of the OTF. Accordingly to Equation 3.2, the frequencies of the component $C'_{\vec{p}}$ are the projections of the source signal $S(\vec{k} - \vec{p})$ frequencies, as if \vec{p} was the origin of the Fourier transformed sensed signal F . That is, an estimate of the source signal from the information contained in the component $C'_{\vec{p}}$ can be illustratively⁶ written as

$$\hat{S}_{C'_{\vec{p}}}(\vec{k}) \cdot H(\vec{k} - \vec{p}) = C'_{\vec{p}}(\vec{k}). \quad (3.10)$$

As indicated in Item iii. an OTF is assigned⁷ to every component $C'_{\vec{p}}$ of every orientation $n \in [3]$

$$H'_{\vec{p}}(\vec{k}) = H(\vec{k} - \vec{p}).$$

6: The estimate is not obtained in this way precisely as will be demonstrated in Subsection 7.

7: When using a model OTF, this is trivially done by evaluation with translated arguments. If a LR measured transfer function is to be used it must be upsampled due to the mismatch of sampling rates of the HR and LR images, and the translation must be realized using the Fourier shift theorem. Alternatively, the evaluation may be done of an interpolation of the measured data.

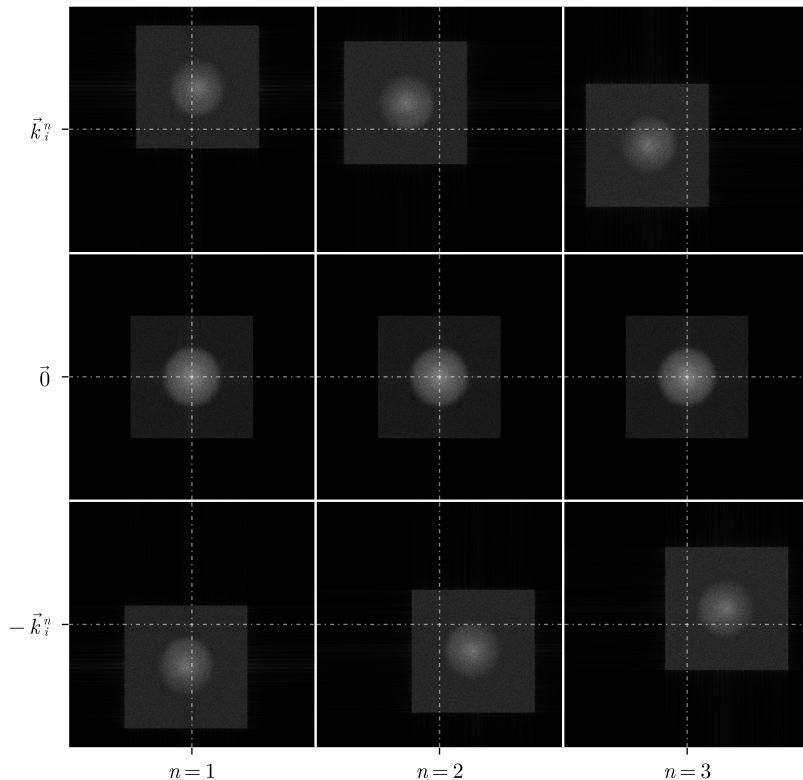


Figure 3.4: The components shifted to their corresponding locations in the HR image.

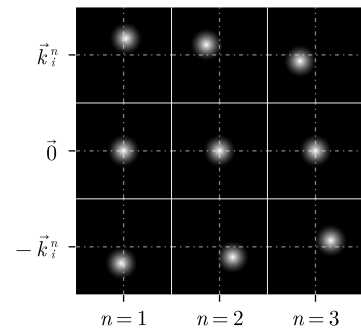


Figure 3.5: OTFs $H'_{\vec{p}}$ of the \vec{p} -shifted components.

Wiener Filter (iv.)

The state of the reconstruction is that we have frequency components, positioned at locations within the Fourier space that are in compliance with the physical structure that they represent in the source signal and have appropriate OTFs for them. Each OTF corresponding to a component acts as degradation function for the source signal S in the components location (Eq. (3.10)). The degradation is embodied by a convolution of the source signal with a point spread function (PSF) or in the frequency space by multiplication with the OTF. Inversion of this degradation process in image processing is called deconvolution (also restoration). There are many approaches with various purposes that attempt to achieve deconvolution each targeted for a different purpose.

One such approach, that is widely used is the *Weiner* deconvolution (filter). It is derived in as a least square error estimate of the original signal, given a noisy sensed signal and a known transfer (degradation) function. A simplified version of the Weiner filter estimate \hat{S} of a noisy signal F and an OTF H is given by

$$\hat{S} = \frac{H^* F}{H^* H + \omega^2},$$

where ω is an empirically chosen real constant, which represents inverse signal-to-noise ratio (SNR) in the noisy signal. For the purpose of restoring the relocated components the estimate is realized using

Figure 3.6: Reconstructed HR image using *Weiner* deconvolution.

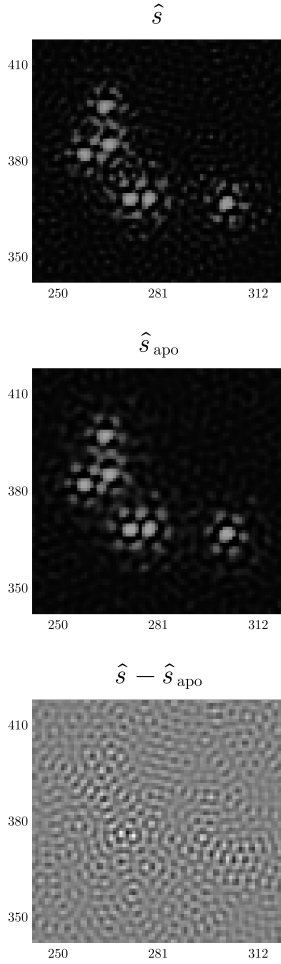
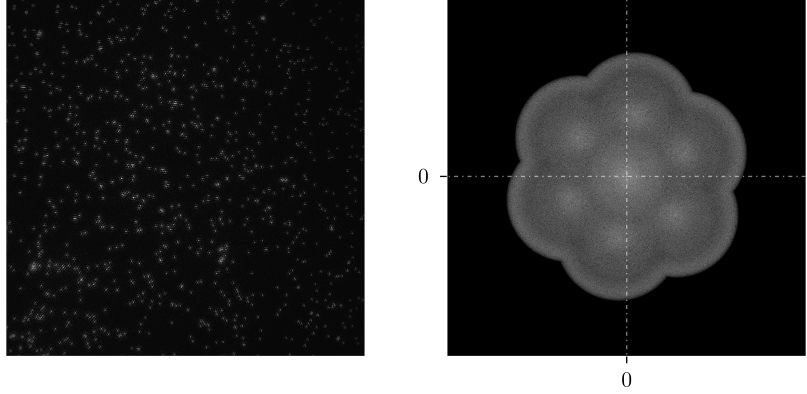


Figure 3.7: At the top the full reconstructed image without any modifications and filtering. There are visible periodic artefacts, in the SIM terminology aptly named *honey comb* artefacts, that are most prominent in the background area of the image. In the middle, the same reconstruction but after performing strong apodization filtering. It is apparent that the apodized image has less artefacts in the background but is also noteworthy, that the image also has a lower resolution that can be observed by comparing the sizes of the beads in the filtered and non-filtered reconstructions. At the bottom, difference between the two reconstructions that accents the form of *honey comb* artefacts.



frequency information from all of the components in the numerator and the full HR image OTF in the denominator

$$\hat{S}_{\text{SIM}}(\vec{k}) = \frac{\sum_{n=1}^3 \sum_{\vec{p} \in \{-\vec{k}_i^n, \vec{0}, +\vec{k}_i^n\}} (H_{\vec{p}}^{n'}(\vec{k}))^* C_{\vec{p}}^{n'}(\vec{k})}{\sum_{n=1}^3 \sum_{\vec{p} \in \{-\vec{k}_i^n, \vec{0}, +\vec{k}_i^n\}} (H_{\vec{p}}^{n'}(\vec{k}))^* H_{\vec{p}}^{n'}(\vec{k}) + \omega^2}.$$

It is visible (Fig. 3.6), in particular in the Fourier domain, that the reconstruction is not optimal (Fig. 3.7). The first aspect that is clearly not expected in an optimal reconstruction are noticeable peaks at the locations of the shift frequencies \vec{k}_i^n for all orientations $n \in [3]$.

There is no physical reason for the presence of these peaks. One explanation is incorrect parameter estimation that leads to an incorrect component separation. This is partly the case as we can see that the left-top and right-bottom components have slightly more prominent peaks than the other two orientations, which suggests that there are "leftover" parts of the central component, which should physically have the strongest intensity within the Fourier domain.

However, this reasoning fails to fully explain the deficiency of the reconstruction which reveals itself by the pronounced circumference of the Fourier spectrum. This cannot be explained by inferior component separation, but instead points toward a suboptimal transfer function used for the reconstruction which admits frequencies that should be dismissed as being beyond the OTF support of the imaging system. We will tackle this issue in Chapter 4.

Apodization

One more tool which commonly gets employed to counter these high-frequency artefacts is apodization of the output Fourier domain HR image. Apodization is in effect a low-pass filter which is constant 1 near the origin and beyond some predefined radius, decreases to 0 according to some smooth function that is termed the *apodization function*. The smoothness of the decrease is important for suppressing the formation of artefacts that occur from using the discrete Fourier transform (DFT) on a signal with abrupt edges. There are many possibilities to use as apodization functions, but in this particular use-case, there is no

significant difference between using any of them. One that is used commonly is the *cosine apodization function*

$$A_a(r) = \cos\left(\frac{\pi r}{2a}\right),$$

where a is a chosen constant parameter of the apodization.

A disadvantage of using apodization for countering these artefacts is that it dismisses the information in the image from the high frequencies and essentially acts as a denoising procedure during which inherently some features of the image are lost. Due to this, correctly determining and eliminating the attributes that cause the formation of artefact in the reconstruction in the first place is regarded as a better, yet more demanding and non-universal, approach. The artefacts that are filtered from the original non-apodized image are shown in Figure 3.7 on a cut-out from the spatial reconstructed image, and the full apodized reconstruction is in Figure 3.9.

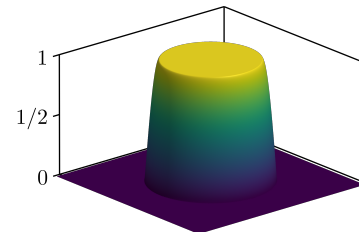


Figure 3.8: The apodization filter used in Figure 3.9.

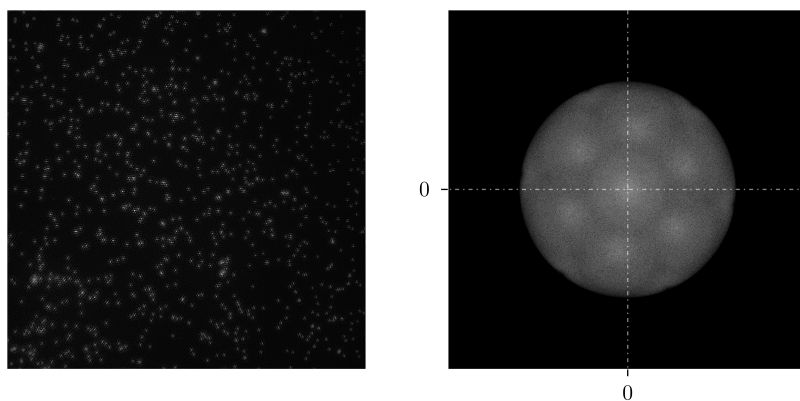


Figure 3.9: Reconstructed image after using apodization to suppress artefacts of incorrect reconstruction parameters and OTF.

3.3 Inversion Reconstruction

The principle of the inversion reconstruction is in many ways easier compared to the Wiener filter reconstruction (Sec. 3.2). It relies on formulating a forward model \mathcal{D} that, when applied to the true source signal s yields the expectation of the sensed LR images \hat{f} . Unlike in the Wiener filter reconstruction, we do not attempt to develop an estimate for \mathcal{D}^{-1} , but instead, it is sufficient to formulate the forward model and rely on mathematical optimization for estimating the correct desired input s , minimizing some defined loss ℓ between $\mathcal{D}[s]$ and the sensed f . A simplified outline of the solution that inversion reconstruction gives is

$$\hat{s} = \arg \min_s \ell[f, \mathcal{D}[s]].$$

Forward Model

The forward model for one LR acquisition f with a specified illumination i_f is apparent from Equation 3.2

$$\hat{f} = (i_f \cdot s) * h, \quad (3.11)$$

where h is the PSF of the optical system. One difference that is necessary to make from Equation 3.11, is, that the optimized \hat{s} must minimize concurrently the loss ℓ for all of the forward model expectations of the LR acquired images at the input, with a single estimate of \hat{s} . An obvious and easiest way to achieve this is to minimize the sum of loss ℓ evaluated for every input image

$$\ell_{\Sigma}[\{f_n\}, \{\mathcal{D}_n[s]\}] = \sum_n \ell[f_n, \mathcal{D}_n[s]].$$

Loss Function

A choice that is necessary to make is, the form of the loss ℓ . The role of the loss function is mapping the parameters of the optimization problem (in our case the values of the pixels of the forward model carried out on the source signal s) onto a real number. The important aspect of loss that is necessary to redeem is, that minimization of the loss leads to a better estimate of the parameters that we want to determine. One very common choice for the loss in deep learning applications is the ℓ_2 norm between the measurement and the prediction. It is possible however, to choose a better loss, that is directly linked to the nature of our optimization problem. An ideal choice is dependent on the nature⁸ of the estimate \hat{s} that we want to achieve. In microscopy (especially in low SNR acquisitions), the dominant source of noise is due to photon (Poisson) shot noise (Sec. 4). Assuming a correct forward model \mathcal{D} , we can specify the probability of a sensed signal in relation to the true source signal s as

$$\mathcal{P}[f | \mathcal{D}[s]] = \prod_{\vec{r}} \frac{(\mathcal{D}[s](\vec{r}))^{f(\vec{r})}}{\Gamma(f(\vec{r}) + 1)} \cdot e^{-\mathcal{D}[s](\vec{r})}.$$

Based on this, assumption, we want to get a reconstruction \hat{s} such that the probability $\mathcal{P}[f(\vec{r}) | \mathcal{D}[\hat{s}](\vec{r})]$ is as large as possible, since this would be the reconstruction that is most probable to describe the sensed LR images f . To reach this goal the loss is set to be the negative log-likelihood⁹ of the sensed LR images (taking e for the base of the logarithm)

$$\begin{aligned} \tilde{\ell}_{\mathcal{P}}[f, \mathcal{D}[s]] &= -\ln(\mathcal{P}[f(\vec{r}) | \mathcal{D}[s](\vec{r})]) \\ &= \sum_{\vec{r}} \mathcal{D}[s](\vec{r}) + \ln(\Gamma(f(\vec{r}) + 1)) \\ &\quad - f(\vec{r}) \cdot \ln(\mathcal{D}[s](\vec{r})). \end{aligned} \quad (3.12)$$

The term $\ln(\Gamma(f(\vec{r}) + 1))$ in the loss of Equation 3.12 is constant for any source s so we can ignore it. The final loss for the optimization problem then becomes

$$\ell_{\mathcal{P}}[f, \mathcal{D}[s]] = \sum_{\vec{r}} \mathcal{D}[s](\vec{r}) - f(\vec{r}) \cdot \ln(\mathcal{D}[s](\vec{r})). \quad (3.13)$$

8: Similarly to mathematical statistics, there is no optimal choice for an estimate. Instead we can choose to value some of its properties such as it being non-biased, its speed of convergence or its robustness to spurious input data (such as outlying measurements). From a standpoint of mathematical optimization, also the numerical stability of the optimization must be taken into account.

9: Using this loss during the optimization, if we disregarded the regularization term (Sec. 9), is equivalent to performing the maximum likelihood estimate (MLE) of the s in mathematical statistics.

Regularization Term

To prevent over-fitting of the reconstructed \hat{s} during the optimization, it is necessary to add regularization to the optimization problem. Regularization leads to a simpler solution, that may be more robust to the unwanted influence of noise that would otherwise be inflicted by the optimization. In general, it is necessary to add some form of regularization into the optimization problem, if the ratio of the number of parameters in the output to number of input data points is large. The principle of regularization is to impose some additional constraint to the output parameters that forces against outputs that would be in conflict with what is physically expected of the output.

Here the regularization is added explicitly in the form of a regularization term. The form of the regularization term can highly influence the output and so it is necessary to choose it carefully. Most regularization terms used in the context of images are defined in favour of the principle, that the output should be reasonably smooth. In other words, it attempts to penalize variation in the output.

One of the most commonly used regularization terms is *total variation (TV)* in the form

$$\text{Reg}_{\text{TV}}[s] = \sum_{\vec{r}} |\nabla s(\vec{r})|,$$

where ∇s is approximated for the discretely sampled s and the resulting formula, for u and v being the pixel indices, is given by

$$\text{Reg}_{\text{TV}}[s] = \sum_{u,v} \sqrt{|s(u+1,v) - s(u,v)|^2 + |s(u,v+1) - s(u,v)|^2}.$$

Another option that is frequently used for images is *Good's roughness (GR)* for which the continuous formula is

$$\text{Reg}_{\text{GR}}[s] = \sum_{\vec{r}} \sqrt{s(\vec{r})} (\Delta \sqrt{s})(\vec{r}),$$

where $\Delta \sqrt{s}$ is the Laplace operator and it is approximated in the discrete domain as

$$\text{Reg}_{\text{GR}}[s] = \sum_{u,v} \sqrt{s(u,v)} \cdot \left(\frac{\sqrt{s(u+u_\Delta,v)} + \sqrt{s(u-u_\Delta,v)}}{u_\Delta v_\Delta} + \frac{\sqrt{s(u,v+v_\Delta)} + \sqrt{s(u,v-v_\Delta)} - 4 \cdot \sqrt{s(u,v)}}{u_\Delta v_\Delta} \right).$$

Optimization

The final reconstruction optimization problem is posed as

$$\hat{s} = \arg \min_s (\ell_\Sigma[\{f_n\}, \{\mathcal{D}_n[s]\}] + \lambda \text{Reg}[s]),$$

where λ is the regularization parameter, that is set empirically and the loss is the sum of Poisson losses ℓ_p .

Figure 3.10: Reconstructed \hat{s} using optimization reconstruction with TV (top row) and GR (bottom row) for regularization and $\lambda = 0.05$. A big difference in the two reconstructions is not visible in this case.

[22]: K Mogensen et al. (2018), *Optim: A Mathematical Optimization Package for Julia*

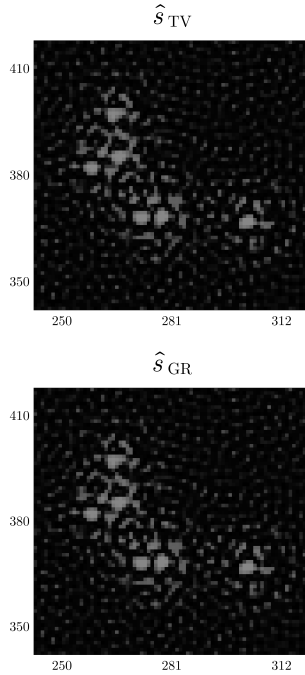
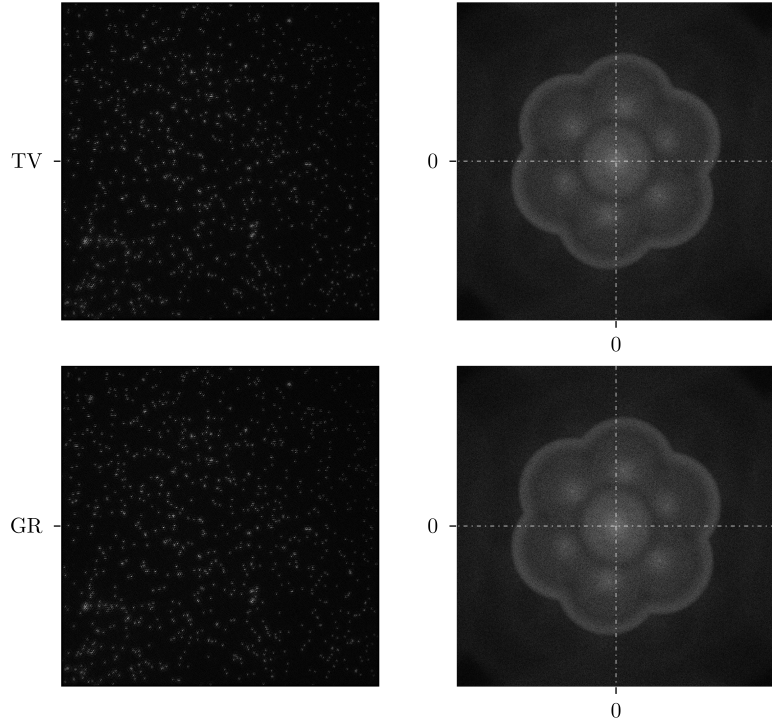


Figure 3.11: Comparison of the two reconstructions using GR and TV for regularization ($\lambda = 0.05$) on a cut-out of the image. It is important to note that λ does not have the same effect for one value on any regularization.



The numerical optimization itself is performed using the limited-memory Broyden–Fletcher–Goldfarb–Shanno (L-BFGS) algorithm similar to gradient descent with the use of source-to-source backward propagated automatic differentiation for computing the gradient and Hessian [22].

3.4 Discussion

There has been a lot of research on the use of different reconstruction methods and their benefits have been demonstrated on particular datasets. To this date, no reconstruction method has been distinguished as the "holy grail" that is best for any dataset universally, as is often the case for any set of algorithms developed for a particular purpose. Benefits can be attributed to each method. More limiting are the drawbacks that may deem an approach utterly inappropriate for a particular methodology of observation.

One such example is the use of machine learning based methods. The major drawback that they inherently possess is the lack of fidelity of the output. This is due to the way machine learning methods work in most implementations. Usually the training dataset is generated by modifying the source similarly to how it was expressed in Subsection 3.3 and the user formulating a procedure to generate model sources s that are applicable for the given observation. Generating the training dataset in this manner ensures that the learning can be supplied with a ground truth of the source signal. This means that the training dataset is not necessarily natural in the sense that the data used for training may not be variable enough to encompass the structure of the real world data input for reconstruction and the resulting model can be biased in the direction of data that it was supplied with during training.

The quality of the model that is problematic in this regard is termed in literature as the *ability of the model to generalize* and although it is possible to minimize the issue to a certain extent, it is always present at some degree. Due to this, machine learning methods are hard to justify in the reconstruction of biological structures which are not yet fully understood to the level of being able to generate models of their structure that are absolutely dependable. On the other hand, the fact that the reconstruction is "aware" of the source structure that it should output can lead to machine learning reconstructions, that use appropriate source models, to be vastly less noisy and visually and structurally more appealing than reconstruction based on other methods.

Another benefit is that the reconstruction using machine learning can be supplied with data without any preparation steps. Denoising and other procedures that ensure the visual quality of the reconstruction can be incorporated into the reconstruction step itself which means that there is no information lost before the actual reconstruction is performed. In general, there is a trend for new algorithms to consolidate all the steps into one single model precisely due to this reasoning.

An aspect that must be considered when choosing a reconstruction method, if the object of the observation is not static (e.g. *in vivo* acquisitions), is the value of temporal resolution and the photon efficiency of the observation. There is an intrinsic deficiency of the Wiener filter reconstruction in the fact that it is necessary to sense the image 3 times in a single orientation to be able to linearly separate the components. Machine learning and optimization based reconstruction procedures do not possess this limitation, as long as we are able to estimate the parameters of the illumination patterns. This can be recognized from the Equation 3.1, which suggests that we gain no additional information from the two additional acquisitions having different phase-offsets. An equivalent optimization reconstruction is therefore in theory possible to perform using only 3 LR images, one for each orientation (Fig. 3.12). The difference in these two reconstructions should be explainable only through the additional optimization parameters that should benefit the robustness towards noise.

A further, very interesting, possible enhancement to the machine learning and optimization approaches is to apprehend the estimated parameters of the illumination pattern as random variables with a certain distribution instead of constant estimates or to perform the estimates as part of the reconstruction. That can be leveraged in the reconstruction to further fine tune the properties we are expecting from the output without overly relying on the correctness of the estimates. Within the machine learning approach this can be achieved by training the reconstruction model without supplying the correct parameters as part of the data. For the optimization reconstruction, this can be done by Bayesian inversion [23] using Bayes rule in the form

$$\mathcal{P}[s, \lambda | f] = \frac{\mathcal{P}[f | s, \lambda] \cdot \mathcal{P}[s, \lambda]}{\mathcal{P}[f]},$$

where λ are the parameters of the illumination patterns during acquisition of f $\mathcal{P}[s, \lambda] = \mathcal{P}[s] \cdot \mathcal{P}[\lambda]$ due to independence, $\mathcal{P}[s]$ can be set

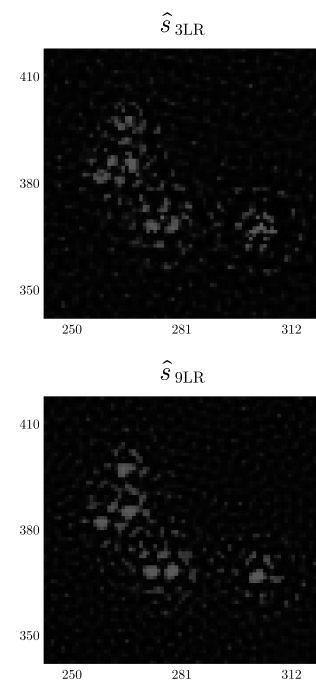


Figure 3.12: Comparison of optimization reconstruction performed from 3 and 9 LR images.

[23]: Orioux et al. (2012), *Bayesian Estimation for Optimized Structured Illumination Microscopy*

either as the uninformative prior or as a conjugate prior to the noise distribution $\mathcal{P}[f | s, \lambda]$ and the prior $\mathcal{P}[\lambda]$ can be formed by randomizing the parameter estimates.

One hybrid approach to integration of parameter estimation into the reconstruction is tiled SIM reconstruction. The idea is that the LR images are subdivided into tiles and the reconstruction is performed for each tile individually. The parameters are estimated independently for the tiles. This has been shown to lead to better results in some cases [24].

[24]: Hoffman et al. (2020), *Tiled Reconstruction Improves Structured Illumination Microscopy*

Measurement of the Transfer Function

4

If we have an optical system and want to model the way light passes through that system, either in order to enhance our estimate of the structure (source) that causes the output signal or to establish characteristics of that system, we need to determine one of the transfer functions of the optical system. Of the transfer functions, it is most intuitive to directly measure the PSF or more specifically the magnitude of the PSF. We disregard the phase change that the optical system may introduce, because in most set-ups it is practically impossible to directly measure the imaginary part of the PSF¹, since the light sensors (In our case the complementary metal–oxide–semiconductor (CMOS)) only measure the energy that hits the sensor elements which is equivalent for all possible phases of the EM wave, since it only depends on the intensity of the EM wave (Chap. 1).

For estimating the transfer function, it is necessary to make an acquisition of a known source signal. It is possible to categorize the following methods of estimation into two parts. At first, we will avoid creating a model of the whole source image s and only leverage the knowledge of the objects that are being observed. For this, a more comprehensive formulation of the image formation will be discussed in Section 4.1 and then the model-free estimate of the PSF will be performed (Sec. 4.2). Next, a complete model \hat{m} of the source signal s will be determined (Sec. 4.3) and a method for estimation of the OTF using this model will be demonstrated. Afterwards, one more estimate of the PSF that leverages the model and recognizes the fact that the data is from a SIM acquisition will be performed (Sec. 4.5) Finally, we will return to the topic from Chapter 3 and compare the reconstructions that use the transfer function estimates from this chapter (Sec. 4.6).

4.1 Image Formation Model

Devising an image formation model means to formulate the manner in which, we expect light from the source to manifest itself in the resulting sensed signal. For reasoning about the later estimates of the transfer functions, it is necessary to express this image formation model mathematically. It is sensible to proceed in the same chronological order as the light passing through the apparatus. With this in mind, we will start off with the illumination of the focal plane.

Illumination

The transfer function of the optical system, is given by measuring the way that light passes through the apparatus given a uniformly illuminated focal plane. However, we do not have data directly observed using a regular uniformly illuminated wide field microscopy system. Our images are acquired with the harmonic illumination (Chap. 2). This

| | |
|--|-----------|
| 4.1 Image Formation | 35 |
| Illumination | 35 |
| Noise | 36 |
| The Transfer Function | 39 |
| The Source | 40 |
| 4.2 PSF from Beads | 41 |
| 4.3 The Source Model | 43 |
| Single Bead Model (i.) | 43 |
| Locating the Beads (ii.) | 44 |
| 4.4 Estimating the PSF from the Model | 47 |
| 4.5 PSF from SIM | 47 |
| 4.6 New Reconstruction | 47 |
| 4.7 Discussion | 50 |

1: It is possible in some cases to determine the imaginary part (i.e. the phase change PSF) from the magnitude PSF algorithmically if we assume certain properties of the complex PSF. This algorithmic restoration of the phase is called phase-retrieval. However, in order for the phase to be unambiguous, thus for the phase-retrieval algorithm to be stable, it is necessary that the phase retrieved function to be non-symmetric with respect to the origin, which is often the case for the PSF [25]. There are other algorithms that for phase retrieval that leverage the fact that the prior knowledge of the PSF [26].

[25]: Goodman (2005), *Phase Retrieval from Fourier Magnitude*

[26]: Hanser et al. (2003), *Phase Retrieval for High-Numerical-Aperture Optical Systems*

2: Meaning that the source of the light is stationary in contrast to *in vivo* biological acquisitions, where this is not the case.

3: In accordance with the method that is used to generate the patterns in the case of our SIM setup, we are assuming that the phases differ by $2\pi/3$ from one another and do not determine them independently (Sec. 3.1).

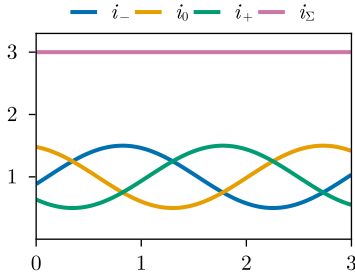


Figure 4.1: Sum of the illumination pattern intensity along the wave vector for the first orientation, results in a uniform intensity.

4: This assumption holds precisely if the illumination pattern is generated by a diffraction grating, which is our case, and also theoretically if laser interference is used.

5: The location in the apparatus in which noise corruption happens is particularly interesting for the purpose of estimating the transfer function, because if the noise is added to the signal before the pass through the optical system, it is degraded with the transfer function along with the signal and if the corruption happens after, the noise affects the already degraded signal and is independent of the transfer function. As a simplification measure, and in compliance with the major sources of noise, we will only regard noise that corrupts the signal after the pass through the optical system.

6: It is not uncommon to choose to model the noise by a Gaussian distribution ($\mathcal{P} \equiv \mathcal{N}$) even if the Gaussian distribution is physically unrealistic for the given noise source. This assumption is often made for the purpose of simplifying computation.

means that for a still² image, we have 9 wide field images with 3 different pattern orientations and 3 different phases³ for each of those.

In order to account for this discrepancy, we will emulate the uniform illumination by summing all the images acquired with different illuminations together (this will also reduce noise (Sec. 4)). Due to additivity of the optical system, this results in the same signal, as if an acquisition was made with the sum of the illumination patterns. For three patterns in one orientation i_- , i_0 and i_+ , where the phases are $\phi_0 - \frac{2\pi}{3}$, ϕ_0 and $\phi_0 + \frac{2\pi}{3}$, let us, without loss of generality, assume that $\phi_0 \equiv 0$ (since we can move the origin as we please), simplifying the sum i_Σ (Fig. 4.1) along the line of the wave vector of the harmonic pattern i.e. $\vec{r} = \alpha(\vec{k}_i)^\top$, gives

$$\begin{aligned} i_\Sigma(\vec{r}) &= \sum_{i=1}^3 1 - \frac{m_i}{2} \cos\left(2\pi \vec{k}_i \cdot \vec{r} + \frac{2\pi i}{3}\right) \\ &= 3 - \sum_{i=1}^3 \frac{m}{2} \cos\left(2\pi \vec{k}_i \cdot \vec{r} + \frac{2\pi i}{3}\right) \\ &= 3 - \frac{m}{2} \cos(2\pi \vec{k}_i \cdot \vec{r}) \underbrace{\sum_{i=1}^3 \left(\cos \frac{2\pi i}{3}\right)}_{=0} \\ &\quad - \frac{m}{2} \sin(2\pi \vec{k}_i \cdot \vec{r}) \underbrace{\sum_{i=1}^3 \left(\sin \frac{2\pi i}{3}\right)}_{=0}, \end{aligned}$$

where, in the second step, we made the assumption that $m_1 = m_2 = m_3$ ⁴.

Noise

As a first step towards developing a faithful image formation model of a uniformly illuminated source, we need to consider noise.

The mode of noise, that we will be particularly interested in is *additive noise*, for which the strength of the noise is added to the noise free source signal⁵:

$$f(\vec{r}) = \overbrace{g(\vec{r})}^{\text{signal}} + \underbrace{\eta(\vec{r})}_{\text{noise}}. \quad (4.1)$$

Additionally, in Equation 4.1 the noise $\eta(\vec{r})$ has a specified distribution⁶

$$\eta(\vec{r}) \sim \mathcal{P}_{\vec{r}},$$

where we often assume that the distribution is location independent (i.e. $\mathcal{P}_{\vec{r}} \equiv \mathcal{P}$). An important property to consider when characterising noise from different sources is *signal independence*, i.e. whether the strength of the noise is independent from the intensity of the signal in the sense of a random variable

$$\{\eta(\vec{r}) \mid g(\vec{r})\} = \eta(\vec{r}).$$

There are many sources of noise that should be considered in the acquisition model. The most prominent of these sources are caused by the image sensor (the CMOS), especially in low SNR acquisitions.. It is also common to regard the variations in the ambient (background) illumination i.e. the light that is not part of the source we are measuring as noise. The sources, that are the greatest contributors to the noise corruption of the expected signal are:

Photon noise Inherent to the quantized nature of energy transmission of light. Sensors measure irradiance by counting the number of discrete photons that land on the sensor in a given time interval $\Delta\tau$. The arrivals of individual photons are independent and can therefore be regarded as a Poisson process. The number N of photons detected in the time interval $\Delta\tau$ can thus be described by the distribution (Fig. 4.2)

$$\mathcal{P}[N = x] = \frac{e^{-\lambda'} \Delta\tau (\lambda' \Delta\tau)^x}{x!},$$

where the rate parameter λ' corresponds to the expected incident photon count per unit time, i.e. the expected number of photon detections per a unit of time. It is dependent on the source luminance. Since $\mathbb{E}N = \text{Var}(N) = \lambda' \Delta\tau =: \lambda$, the ratio of signal to noise increases with $\sqrt{\lambda' \Delta\tau}$ and so the corruption due to this source of noise is greatest in situations with low signal levels. For larger counts of photons, we can use the central limit theorem to approximate the photon noise by a Gaussian additive noise [27], whose variance and mean both depend on the signal luminance level

$$\eta(\vec{r}) \sim \mathcal{N}(\lambda'(\vec{r}) \cdot \Delta\tau, \lambda'(\vec{r}) \cdot \Delta\tau).$$

Dark current Semiconductor detectors in the image sensor are susceptible to thermal agitation [5], which can cause the photocapacitors to charge even in the absence of light (hence the name dark current) leading to false signals. Due to the phenomenon of dark current, the sensors are often cooled during acquisition to reduce this effect. Noise from this source is signal independent and additive.

Background noise Additive and independent noise from the ambient light that reaches the sensor or unwanted light caused by other effects. An example can be the lagged emission of the fluorescent proteins. This effect of ambient light from outside sources is most prominent for low energy light (i.e. light with low frequencies, e.g. infrared light), which is more prone to scattering and harder to effectively suppress. In the case of biological sensing however, a majority of what we consider background noise comes from the light that is far from the focal plane and defocus causes it to blur and appear as ambient light with locally (meaning in a small bounded region) limited variation. This is the principal reason for the use of a TIRFM setup.

Auxiliary sources A variety of causes, mainly in the imaging sensor, that are produced at the read-out time⁷. Notably the charge transfer in the CMOS sensor can be the cause of noise although, modern CMOS sensors are seeing much improvement in this direction in the recent past [28]. Auxiliary sources can be both signal dependent and independent.

A popular measure used in signal processing to quantify the relative power of noise is the SNR. For an image it is defined as

$$\text{SNR} = \frac{\sum_{u,v} |g(u,v)|^2}{\sum_{u,v} |\eta(u,v)|^2}.$$

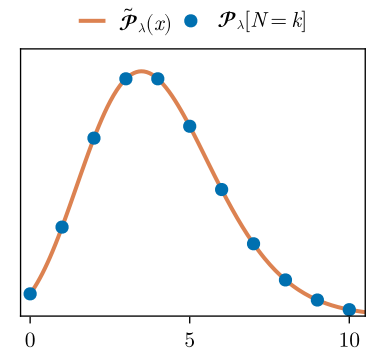


Figure 4.2: The Poisson distribution and its continuous equivalent

$$\tilde{\mathcal{P}}_{\lambda}(x) = \frac{e^{-\lambda} (\lambda)^x}{\Gamma(x+1)},$$

for $\lambda = 4$.

[27]: Hasinoff (2021), *Photon, Poisson Noise*

[5]: Aguet (2009), *Super-Resolution Fluorescence Microscopy Based on Physical Models*

7: The phases after the photo activation of the sensor elements (consisting of amplification, digitization of the analog signal etc.).

[28]: Holst (2014), *Scientific CMOS Camera Technology: A Breeding Ground for New Microscopy Techniques*

If we know or assume a distribution of additive noise, it is possible to estimate its parameters using regions of the image with approximately or theoretically constant intensity (e.g. background regions)

$$A := \{\vec{r} \mid g(\vec{r}) \approx c\}.$$

It is often the case that we assume, or in approximation assume, that the distribution of the additive noise is Gaussian and we can estimate the parameters of the noise using the for example MLE

$$\hat{\mu}_\eta = \frac{1}{|A|} \sum_{\vec{r} \in A} (f(\vec{r}) - c)$$

$$\hat{\sigma}_\eta^2 = \frac{1}{|A|} \sum_{\vec{r} \in A} (f(\vec{r}) - \hat{\mu}_\eta)^2.$$

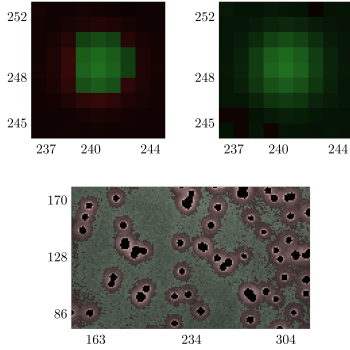


Figure 4.3: The windowed Otsu threshold leads to lower intensities of some beads to be passed as background. On the left, side, Otsu threshold $t_o(\vec{r})$ is used for classifying the image pixels into background and foreground by selecting the locations which have a higher intensity than $t_o(\vec{r})$. On the right, the threshold is lowered to $\tilde{t}_o(\vec{r}) := 0.3 \cdot t_o(\vec{r})$ and the same classification is performed. At the bottom, difference between rejected pixels by t_o and accepted by \tilde{t}_o as foreground are shown.

[29]: Otsu (1979), *A Threshold Selection Method from Gray-Level Histograms*

[30]: Foi et al. (2008), *Practical Poissonian-Gaussian Noise Modeling and Fitting for Single-Image Raw-Data*

Moreover, if the limitation to the theorized noise distribution is to be avoided, it can be eyeballed from the histogram or the histogram, kernel or other empirical estimate of the intensity distribution within A can be used.

In our case, the premise that allows us to select such a set A is the lack of other non-ambient signal sources besides the beads. The problem therefore reduces to the distinction of the beads from the background, for which we can use the Otsu threshold [29], which minimizes the intra-class variance for two classes of within the image

$$t_o = \arg \min_t (|\{f(\vec{r}) \mid f(\vec{r}) > t\}| \cdot \text{Var}\{f(\vec{r}) \mid f(\vec{r}) > t\} + |\{f(\vec{r}) \mid f(\vec{r}) \leq t\}| \cdot \text{Var}\{f(\vec{r}) \mid f(\vec{r}) \leq t\}).$$

It is not effective, though, to use the global Otsu threshold, because the image does not have a uniform distribution of intensity due to the aberrations and vignetting and partly due to the varying concentration of beads within the image source. What turns out to be a better choice is a windowed Otsu threshold determined for each pixel. Even with this enhancement though, the threshold does not achieve to completely eliminate the lower intensities at the edges of beads from the background which we want to determine (Fig. 4.3). Because background covers the majority of the image region and we have a lot of data points available to estimate the noise distribution from, we can afford to reduce the threshold for the benefit of only accepting noise at the cost of rejecting some of the background in the process. Empirically the choice was for the final lowered windowed threshold to be

$$\tilde{t}_o = 0.3 \cdot t_o,$$

which is used in the thresholding for estimation of A , the background.

A well established model of the noise distribution that is used in low SNR acquisitions is noise consisting of two components that are assumed to be independent. A Poisson distributed signal-dependent component $\eta_{\mathcal{P}}$ that represents the photon shot noise and a Gaussian signal-independent component $\eta_{\mathcal{N}}$ for the read-out noise [30]. An a and b parametrized formulation of the model that we are to estimate can be written as

$$\eta_{\mathcal{P}}(\vec{r}) = \frac{1}{a} \cdot \alpha(\vec{r}) \quad \alpha(\vec{r}) \sim \mathcal{P}(a \cdot g(\vec{r}))$$

$$\eta_{\mathcal{N}} = \beta \quad \beta \sim \mathcal{N}(0, b^2) \quad (4.2)$$

$$\eta(\vec{r}) = \eta_{\mathcal{P}}(\vec{r}) + \eta_{\mathcal{N}}.$$

For the estimate of this model, it is easiest to assume some form of the noise-free signal g .

We selected A as the background exactly for the reason that we may

make some deductions about g within the region of A . Unfortunately the assumption stated as a premise for selecting A as the appropriate region was too crude. It is not viable to assume that $g(\vec{r}) \equiv 0$ for $\vec{r} \in A$ according to the premise, because of the ambient light background noise. We will estimate the ambient light background \hat{g} that will play the role of g within A by taking a windowed mean of the background regions (Fig. 4.4).

There is an unequivocal scheme for roughly verifying the sensibility of the model (Eq. (4.2)) taking the advantage of additivity of the Poisson and Gaussian distributions

$$\begin{aligned} X \sim \mathcal{N}(0, \sigma_X^2), Y \sim \mathcal{N}(0, \sigma_Y^2) &\implies X + Y \sim \mathcal{N}(0, \sigma_X^2 + \sigma_Y^2) \\ X \sim \mathcal{P}(\lambda_X), Y \sim \mathcal{P}(\lambda_Y) &\implies X + Y \sim \mathcal{P}(\lambda_X + \lambda_Y). \end{aligned} \quad (4.3)$$

The verification is done by inspecting the histogram of $f(\vec{r}) - \hat{g}(\vec{r}) = \hat{\eta}(\vec{r})$ for $\vec{r} \in A$, which according to Equation 4.3 should be a mixture of the Poisson and Gaussian distributions (Fig. 4.5) in the form

$$\begin{aligned} \sum_{\vec{r} \in A} \eta(\vec{r}) &= \sum_{\vec{r} \in A} \eta_{\mathcal{P}}(\vec{r}) + \sum_{\vec{r} \in A} \eta_{\mathcal{N}} = \frac{1}{a} \cdot \sum_{\vec{r} \in A} \alpha(\vec{r}) + \sum_{\vec{r} \in A} \beta \\ \sum_{\vec{r} \in A} \alpha(\vec{r}) &\sim \mathcal{P}\left(a \cdot \sum_{\vec{r} \in A} g(\vec{r})\right) \\ \sum_{\vec{r} \in A} \beta &\sim \mathcal{N}(0, |A| \cdot b^2) \end{aligned}$$

An estimate is made using the unbiased cumulant estimates from the data [31].

It is practical to assume that the, yet unknown, source signal $s(\vec{r})$, is directly proportional to the concentration of the fluorescent molecules, which in turn is directly proportional to their illuminated volume. For this, it is necessary, that, besides the background noise⁸, to disregard the noise sources, which arise at the source level. This is a reasonable proposition, owing to the fact, that most of the noise can be attributed to the sensor and is added to the sensed signal after the pass through the optical apparatus.

The Transfer Function

Next step is to consider how the source signal $s(\vec{r})$ is affected by the pass through the optical system. As a reminder, in general, for a linear system \mathcal{H} , the Fredholm equation of the first kind applies $\forall \vec{r} \in \mathbb{R}^2$

$$\begin{aligned} g(\vec{r}) &= \mathcal{H}[s(\vec{r})] = \mathcal{H}\left[\iint_{\mathbb{R}^2} s(\vec{x}) \delta(\vec{r} - \vec{x}) d\vec{x}\right] \\ &= \iint_{\mathbb{R}^2} s(\vec{x}) \mathcal{H}[\delta(\vec{r} - \vec{x})] d\vec{x} = \iint_{\mathbb{R}^2} s(\vec{x}) h(\vec{r} - \vec{x}; \vec{r}) d\vec{x}, \end{aligned} \quad (4.4)$$

or without the focal plane simplification $\forall \vec{r} \in \mathbb{R}^3$

$$g(\vec{r}) = \iiint_{\mathbb{R}^3} s(\vec{x}) h_3(\vec{r} - \vec{x}; \vec{r}) d\vec{x},$$

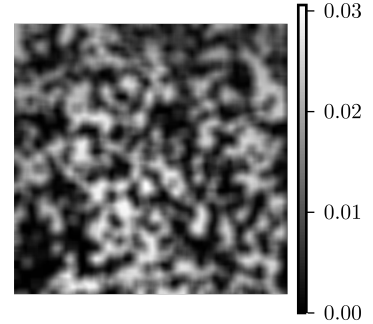


Figure 4.4: The estimate \hat{g} using the windowed mean of the background.

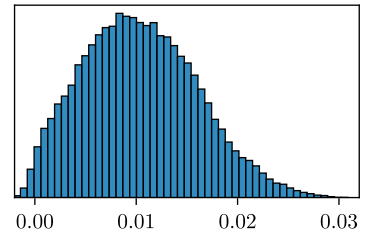


Figure 4.5: The histogram of $f(\vec{r}) - \hat{g}(\vec{r})$ for $\vec{r} \in A$. The Poisson component of the histogram is apparent which should in part imply that the Gaussian component does not play a large role in our acquisition (i.e. that $b \ll a$).

[31]: Bahler et al. (2022), *PoGaIN: Poisson-Gaussian Image Noise Modeling From Paired Samples*

8: Which can be reasonably well removed, but it is important to note that only the power of the noise, linked to the mean value, is effectively reduced, not the variation as such. Methods of removing the background noise generally remove the low spatial frequencies, however the background noise is also prone to the photon shot phenomenon and other signal dependent noise sources, which reside even after the background removal.

where we are using the same notation as in Equation 4.1 and

$$h(\vec{r} - \vec{x}; \vec{r}) := \mathcal{H}[\delta(\vec{r} - \vec{x})]$$

denotes the PSF.

Estimating the PSF h that is location dependent like in Equation 4.4 is badly conditioned, so we need to restraint ourselves to a model or a simplification of the transfer. One option to handle this, is to make the assumption that the system is aplanatic⁹. This assumption makes the PSF focal plane location independent i.e. $\forall \vec{x}, \vec{r} \in \mathbb{R}^2$

$$h(\vec{r} - \vec{x}; \vec{r}) = h(\vec{r} - \vec{x})$$

within the same z -offset plane from the focal plane¹⁰.

For the location invariant h , we can rewrite Equation 4.4 as

$$g(\vec{r}) = \iint_{\mathbb{R}^2} s(\vec{x})h(\vec{r} - \vec{x}) d\vec{x} = (s * h)(\vec{r}), \quad (4.5)$$

where $*$ denotes the convolution operation. The locality¹¹ of the convolution is key to making the PSF more intuitive and easier in practice to measure. It is, because unlike the OTF, we are not forced to make the estimate from the full image or strenuously map the frequency domain of the parts used for measurement onto the frequencies of the acquisition image. Consequently, parts that are easiest to work with can be selected. This can be beneficial in eliminating noisy or inconsistent data, or data, that our model does not consider.

The Source

In order to devise h from Equation 4.5, it is necessary to determine $s(\vec{r})$, for the parts that are used for the measurement. Consider what it would mean for the acquisition, if $s = \sum_{\vec{a} \in A} \delta_{\vec{a}}$. The sensed image, where noise is disregarded, would be

$$g(\vec{r}) = (s * h)(\vec{r}) = \left(\left(\sum_{\vec{a} \in A} \delta_{\vec{a}} \right) * h \right) (\vec{r}) = \sum_{\vec{a} \in A} h(\vec{r} - \vec{a}), \quad (4.6)$$

and if adapted to the more natural notation, where we emphasize, which point underlines the term of the expansion in the image formation formula, i.e. $h(\vec{r} - \vec{a}) =: h_{\vec{a}}(\vec{r})$, Equation 4.6 changes to

$$g(\vec{r}) = \sum_{\vec{a} \in A} h_{\vec{a}}(\vec{r}), \quad (4.7)$$

and we see that the noise-free sensed signal is merely a set of copies of the PSF at the locations of the initial δ sources.

In practice, this type of source is generated by imaging microspheres most commonly made from plastics, stained with fluorescent dyes. Acquisitions of fluorescent beads is often used by biologists for many purposes such as calibrating equipment, because it is possible to manufacture them with a high degree of precision and modeling the source

9: An optical system, or more specifically the lens configuration is aplanatic, if it is free of both spherical and coma aberrations. The aplanatic system assumption is not fully justified and there is a slight location dependence in practice. This issue can be addressed by estimating the PSF on patches of the sensed image separately. This will be done in later sections.

10: However it is important to realize that it is not true that under the assumption of an aplanatic system that PSF h_3 is identical as a function $\mathbb{R}^3 \rightarrow \mathbb{R}$ for the whole imaged volume. The lack of spherical aberration and coma only fixes h on the x and y axes of the object space, so for $\vec{x}, \vec{r} \in \mathbb{R}^3$

$$h_3(\vec{r} - \vec{x}; \vec{r}) \equiv h_3(\vec{r} - \vec{x}; z).$$

11: Locality is understood here as the property that if $\text{supp}(h) \subset \mathcal{B}_\alpha$, then for a source s for which $\text{supp}(s) \subset \mathcal{B}_\beta$ we there exists a γ such that $\text{supp}(s * h) \subset \mathcal{B}_\gamma$.

Equation 4.7 is also applicable for the non-aplanatic transfer, but it is important to realize that in that case the index \vec{a} of the PSF does not denote only a change in coordinates (translation by \vec{a}), but also the change in the function $h_{\vec{a}}$ itself.

that is generated by them is straightforward as we will observe in Section 4.3.

An important aspect that is essential to be able to measure the PSF in a direct manner is that the diameter of the bead is sub-diffraction-resolution¹². If the diameter were not to be sub-diffraction-resolution the source signal would be different from the $\delta_{\vec{a}}$ of Equation 4.6, but rather some other support limited source for which a model $\hat{s}_{\vec{a}}$ would be necessary to develop, and the noise-free sensed signal g would not be direct copies of the PSF h but

$$g(\vec{r}) = \sum_{\vec{a} \in A} (\hat{s}_{\vec{a}} * h)(\vec{r}) \quad (4.8)$$

instead. Deriving the PSF h from the signal in Equation 4.8 would require deconvolution of the individual components $(\hat{s}_{\vec{a}} * h)$ with the assumed model $\hat{s}_{\vec{a}}$ and due to noise, this would necessarily mean that we would need to make further assumptions either about the deconvolved \hat{h} or the noise.

The acquisition that is used for the PSF estimation is done by imaging a suspension of *TetraSpeck™ microspheres*, 0.1 μm , where the diameter is $0.099 \pm 0.008 \mu\text{m}$ [32], which is safely below the diffraction resolution of

$$\frac{\lambda_{\text{em}}}{2 \text{NA}} = \frac{488 \text{ nm}}{2 \cdot 1.4} \approx 174 \text{ nm} = 0.174 \mu\text{m}.$$

4.2 PSF from Beads

It is common in among biologists to select the sensed signal produced by one bead near the centre of the acquisition image and pronounce it as the PSF of the optical system. There is ample room for improvement from this approach. Noteworthy drawbacks of this approach are that

- (a) noise contained in a single bead sample can be substantial,
- (b) the bead centre may not be exactly located at the centre of a pixel and therefore the PSF might be biased,
- (c) it disregards the dependence on the z -offset from the focal plane of the particular bead sample used,
- (d) it is negligent towards the potential dependence of the sampled bead position within the focal plane.

A simplest alternative that addresses all of the aforementioned drawbacks and fixes most of them to certain extent is averaging multiple bead samples. The steps of performing an estimate from multiple bead samples are:

- i. Selecting approximate centres C of isolated beads with the highest intensity¹³.
- ii. Cutting a patch around each centre \vec{c}_i containing the whole bead sample.
- iii. Subtracting the ambient light background from each patch. The intensity of the ambient light in the location of the bead is estimated by the 0.15 quantile of the intensities of a larger patch around the bead sample.

12: It is possible, and even beneficial if the diameter is not sub-pixel-resolution, but it does not make a difference in the principle of the PSF measurement.

[32]: Smith (2020), *TetraSpeck™ microspheres*, 0.1 μm - *Certificate of Analysis*

13: Beads with the highest intensity can be assumed to have the tip closest to the focal plane of the optical system. Since we are looking for the PSF at the focal plane (i.e. $z = 0$), these beads are selected for the estimate.

14: Any other unimodal function, which has its mode at the origin would suffice. The Gaussian is strategic here, since the PSF has close shape to the Gaussian. In fact, it is often modelled by a it.

- iv. Finding the sub-pixel centres of the beads by least square error (LSE) fitting a Gaussian¹⁴ to the sample array
- v. Shifting by sub-pixel offsets of the estimated beads centres from Item 14 to fix the them to a whole pixel value via Fourier shift theorem.
- vi. Averaging the patch pixels to obtain the PSF estimation.

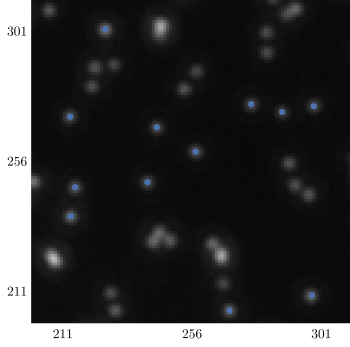


Figure 4.6: Bead samples selected from the center of the image. For better accuracy the locations were selected from the HR reconstructed image.

We subtract the backgrounds of the sample beads before averaging them, therefore, we may assume that their noise is centred, i.e. $\mathbb{E}\eta = 0$. The variance of the PSF values contained in the estimate is reduced regardless of the distribution of the noise in the sensed samples due to the law of large numbers.

We will perform the estimate of the hypothesised focal plane global PSF on bead samples from the center of the image (Fig. 4.6). The cut-outs along with the fitted centres of the bead samples are shown in Figure 4.7. The final PSF estimate and its comparison with the model introduced in Chapter 3 is visible in Figure 4.8.

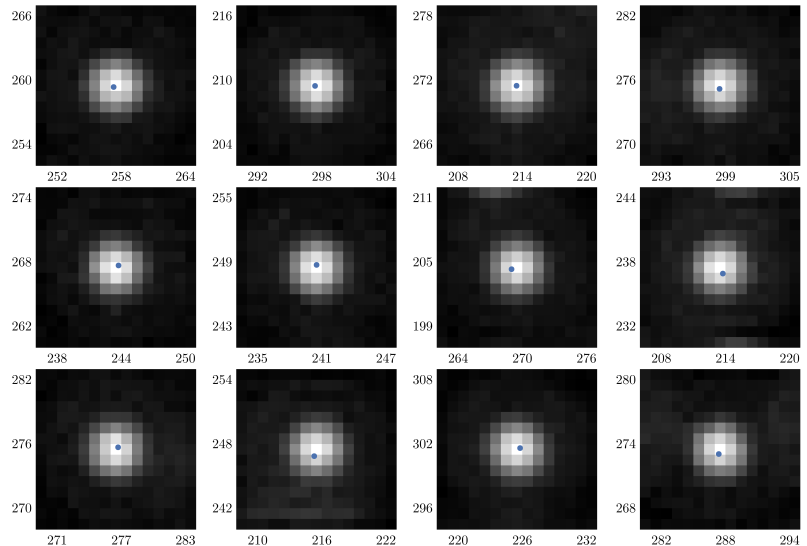


Figure 4.7: The bead samples cut-outs from the center of the image and their fitted centres.

A first test to see if the estimate is better than the proposed model is to compare the deconvolution of the LR image with the proposed PSF (Fig. 4.9). The deconvolution in this case is performed by formulating an optimization problem very similar to the formulation of the optimization problem of reconstruction (Sec. 3.3), with the sole difference that the forward model is the convolution from Equation 4.5 and no regularization is performed. Importantly for assessing the accuracy of the deconvolution, we need to realize, what an ideal deconvolution should look like. The key is that the beads are sub-diffraction-resolution and as such, they should have a single intensity and should be comprehended by the optical system as a single point as defined by the two-point resolution, but they do not have a sub-pixel-resolution so they are supposed to be visible over multiple pixels. The sampling rate of our setup is 61 nm so, since the beads have a diameter of ≈ 99 nm, they should have a image plane diameter of about $1.6 \text{ px}_{\text{LR}}$.

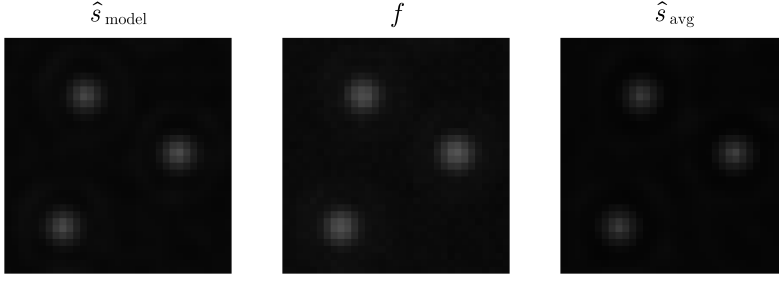


Figure 4.9: Deconvolution of the LR images performed with the PSF model and the PSF estimate. The beads size (99 nm) in the LR sampled (61 nm/px) source should be approximately $1.6 \text{ px}_{\text{LR}}$. The possible explanation for the deviation from this expectation is the varying z -offset from the focal plane which of the individual beads that causes defocus.

4.3 The Source Model

For establishing a model of the source signal, we need to

- i. determine the model of a single bead sampled in the destinations image sampling rate (i.e. for LR images the sampling rate is $61 \text{ nm px}_{\text{LR}}^{-1}$ and for HR images the sampling rate is $30.5 \text{ nm px}_{\text{HR}}^{-1}$)
- ii. find the bead locations within the object field and create the full image model as a sum of the single bead model from Item i. centred at each location.

Single Bead Model (i.)

The beads are effectively balls that are suspended at some z -offset from the focal plane within the object field. We will model them as such balls with a uniform distribution of fluorescent particles at their surface. A simplification that is made is the, not fully accurate, assumption that the z -offset of all the beads is 0 nm. One consideration must be kept in mind and that is the total internal reflection (TIR) nature of the acquisition. This means that the illumination intensity, more befittingly termed excitation intensity in this context, i_{ex} is according to the theory from Chapter 1 attenuated by $e^{\alpha z}$ where α is the attenuation constant that is determined by the super-critical angle of the illumination and z denotes the z -offset from the focal plane of the location of the point in the object field. A full formulation of i_{ex} is therefore

$$i_{\text{ex}}(x, y, z) = i_{\text{ex}}(x, y, 0) \cdot e^{\alpha z},$$

where $i_{\text{ex}}(x, y, 0)$ is constant in our case and can be set to equal 1 without loss of generality to the bead model.

The z -offset of a given patch of the surface of a ball with its tip at the point $(0, 0, 0)$ is

$$z(x, y) = R - \sqrt{R^2 - (x^2 + y^2)},$$

where R is the radius of the ball.

We are working with sub-saturation excitation intensities and time intervals, which means that

$$i_{\text{ex}} \cdot d_{\text{fl}} \propto i_{\text{em}},$$

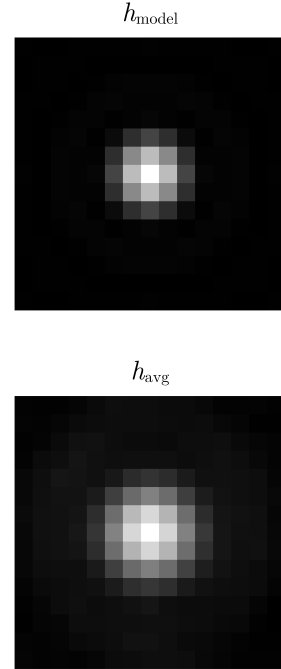


Figure 4.8: The PSF estimate versus the model. The model is clearly wider, which implies that the diffraction-resolution was overestimated by the model which is in line with the reconstruction flaws we discussed in Section 3.2.

where i_{em} is the emission intensity and d_{fl} is the distribution of the fluorescent particles in the object field which was already assumed to be constant for the beads surfaces. This means that the emission intensity i_{em} of a bead at the point (x, y) in the focal plane (Fig. 4.10) is

$$i_{\text{em}}(x, y) = i_{\text{ex}}(x, y, z) = i_{\text{ex}}(x, y, 0) \cdot e^{\alpha z(x, y)} = \frac{e^{\alpha R}}{e^{\alpha \sqrt{R^2 - (x^2 + y^2)}}}.$$

It is crucial to emphasize another simplification that is made and is quite comical considering the goal of developing this model. We are projecting the emission intensity from the (x, y, z) location directly to the emission intensity at the (x, y) location on the focal plane. This is not correct, due to the z -offset plane not having the same transfer function as the focal plane. The major impact of this omission is that we do not consider defocus (as part of the PSF difference) in any way.

The sampling is done by integration of the point emission function $i_{\text{em}}(x, y)$ over the sensor element that corresponds to a given pixel

$$m(u, v) := i_{\text{em}}(u, v) = \iint_{u - \frac{\Delta_x}{2}, v - \frac{\Delta_y}{2}}^{u + \frac{\Delta_x}{2}, v + \frac{\Delta_y}{2}} i_{\text{em}}(x, y) \, dx \, dy,$$

where Δ_x and Δ_y are the dimensions of the sensor element (i.e. the sampling rates in the x and y axes).

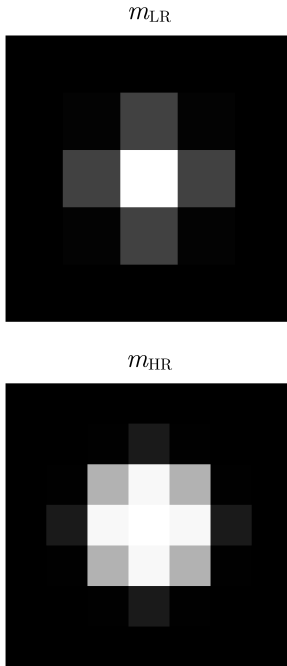


Figure 4.10: LR and HR bead models. The radius of the bead in the LR sampling rate is $\approx 1.6 \text{ px}_{\text{LR}}$, and for the HR bead is $\approx 3.2 \text{ px}_{\text{HR}}$.

Locating the Beads (ii.)

The locations of the beads are determined by an empirically constructed algorithm that is inspired by the general Hough transform and image feature location algorithms. The idea is to

- i. select locations that are candidate to the positions of beads, using a global algorithm with a very low threshold such that no true location of a bead gets discarded,
- ii. filter the candidate locations by a local algorithm to discard the false positives
- iii. determine the final sub-pixel locations of the beads .

The reason for finding the initial candidates by a global algorithm (i.) is induced by the preference of an algorithm that has a simple formulation and for which there is not a overwhelming number of empirical parameters that have to be set. The local filtering of the locations (ii.) is motivated by the fact that the bead samples are typically locally dependent and therefore to robustly discard the false positive locations cannot to be done by comparing all the locations, but only the ones that are comparable with their properties to the one that is being judged, i.e. the locations in the neighbourhood of the bead in consideration.

The global algorithm that is used for selecting the candidates is based on thresholding the cross-correlation of the HR reconstruction \hat{s} with

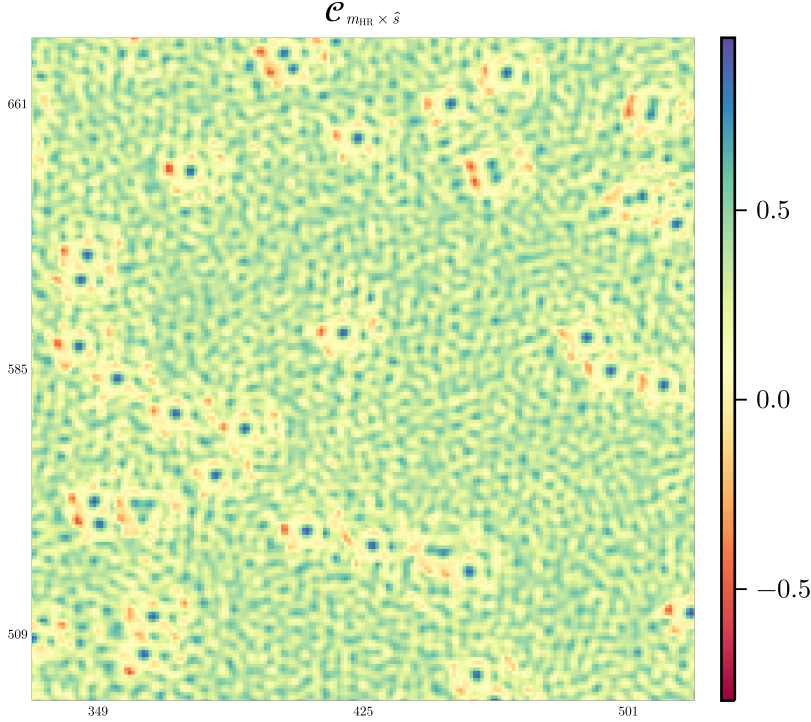


Figure 4.11: Normalized cross-correlation $\mathcal{C}_{m_{HR} \times \hat{s}}$ of the Wiener filter reconstructed HR image with the HR bead model m_{HR} .

[33]: Gonzalez (2008), *Fundamentals of Spatial Filtering*

15: It is often the case that we instead perform the correlation of the demeaned (centred) functions $f - \bar{f}$ and $g - \bar{g}$ in which case the correlation has the meaning of the correlation coefficient and the has values inclusively between -1 and 1 .

the HR bead model m_{HR} (Fig. 4.11) in the form

$$\mathcal{C}_{m_{HR} \times \hat{s}}(u, v) = \frac{\sum_{m, n} \hat{s}(u + m, v + n) \cdot m_{HR}(m, n)}{\sqrt{\sum_{m, n} m_{HR}^2(m, n) \sum_{m, n} \hat{s}^2(u + m, v + n)}}$$

where the limits of summation of m, n are taken to be the overlap regions of the (m, n) -shifted \hat{s} and m_{HR} and \hat{s} is constantly replicated beyond its sampled borders by the border value [33] in order to account for (u, v) in the full sampled area¹⁵. The areas where the cross-correlation $\mathcal{C}_{m_{HR} \times \hat{s}}$ is above $\alpha = 0.62$ are considered to be candidates for beads locations (Fig. 4.12)

$$\mathcal{C}_{m_{HR} \times \hat{s}}(u, v) > \alpha.$$

The filtering of the candidate locations (ii.) is then made by comparing the locations to a wide and narrow neighbourhood mean intensity of the image, \hat{s}_W and \hat{s}_n respectively. In order for the bead region of interest (ROI) to be considered as a true bead ROI and pass to the next filtering step, the ratio of its ROI intensities to the mean intensities must be above some threshold. The comparison with the wide mean of intensity \hat{s}_W is taken with the motivation of discarding the false positive locations that are due to noise that is reminiscent of the bead model. It is made by a windowed mean with a window size of 201×201 px_{HR} and the ideal threshold is empirically determined to be $\beta_W = 8.0$. The final filter (Fig. 4.13) of the candidate ROIs by the wide mean is done as

$$\hat{s}(u, v) > \beta_W \cdot \hat{s}_W(u, v).$$

The comparison with the narrow mean \hat{s}_n is performed in order to

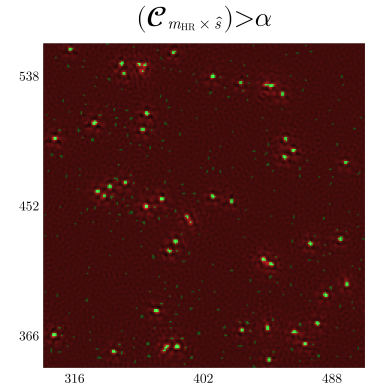


Figure 4.12: The cross-correlation to establish the beads locations candidates. It is visible that some locations within the background are passed as candidates. This is even more pronounced in the distal areas of the image near the edges.

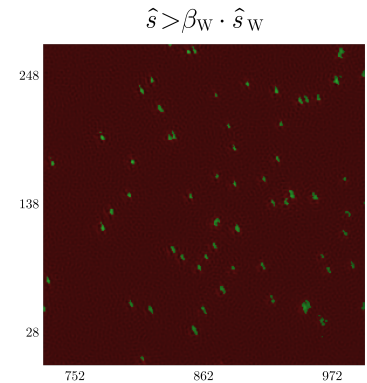


Figure 4.13: The wide mean filter of the candidate bead ROIs. It is effective in discarding the false positive locations that are due to the background noise and therefore have a low intensity in comparison with the mean of their neighbourhood intensities.

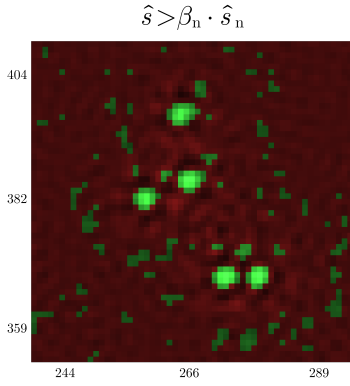


Figure 4.14: In the wide mean, the ROIs of these beads remain connected. This is not desired for in the next step, where the centroids of the ROIs are used as initial locations of the candidate beads for the Gaussian fit. A filter that has a narrow window size is efficient in reducing these connections. Another possibility would be to use the morphological operation of *thinning* [34] on the binary image after the wide mean filter to remove the connections.

[34]: Gonzalez (2008), *Morphological Image Processing*

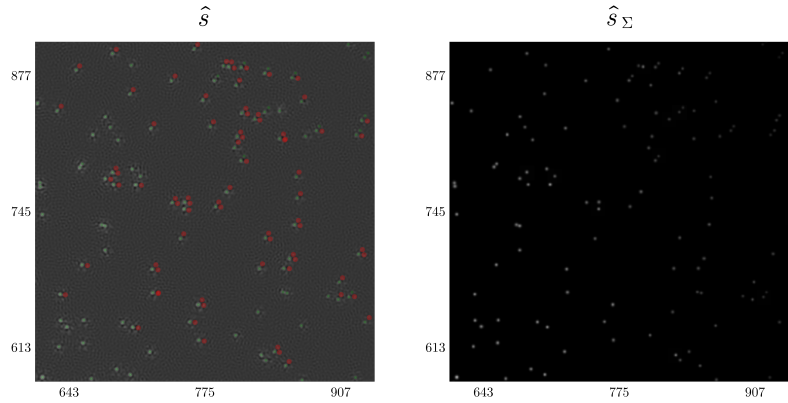
Figure 4.15: Comparison of the reconstructed \hat{s} along with the sum of the fit Gaussian functions for every candidate location and the assumed artefacts are filtered by their location and the relative fitted mean μ and deviation σ . Even though many of the artefact candidate locations are filtered out, the outcome is not ideal and it could be a better strategy to use both the HR reconstructed image for its better resolution and the LR deconvolved image, perhaps in the form of a cross-correlation with the LR bead model to filter out the artefact candidates.

discard the false positive locations that are present because of the reconstruction artefacts that occur using the Wiener filter reconstruction (Sec. 3.2) and to discard the pixels connecting ROIs of beads that are close together, which is necessary for the Item iii.. It is made by a windowed mean with the window size of $15 \times 15 \text{ px}_{\text{HR}}$ and the empirical threshold is determined to be $\beta_n = 2.46$. Similarly to the wide mean threshold, the filtering of the ROIs is done as

$$\hat{s}(u, v) > \beta_n \cdot \hat{s}_n(u, v).$$

The final narrow mean filter that is used on the ROIs of the candidate beads is in Figure 4.14

The sub-pixel center localization (iii.) is performed similarly as in Section 4.2 by fitting a Gaussian to the centroids of the individual ROIs. It assumes that the ROIs of two neighbouring beads does not overlap, which is ensured (at a best effort bases) by setting the thresholds α , β_W and β_n in the previous steps. The fitted Gaussian are further utilized to filter the artefacts that are passed as beads from the previous steps. This is done by setting a threshold on the ratio of means μ and deviations σ of the fitted Gaussian in a neighbourhood and also by noticing that the artefacts are at set relative locations from the bead that causes them (Fig. 3.7).



The final source model (Fig. 4.16) \hat{m} is then obtained by summing the single bead models m_{HR} at the filtered locations, weighted in order for the maximum intensity of the bead at the location to match the intensity of the fitted Gaussian. Weighting is done to account for the different z -offsets as mentioned in Subsection 4.3.

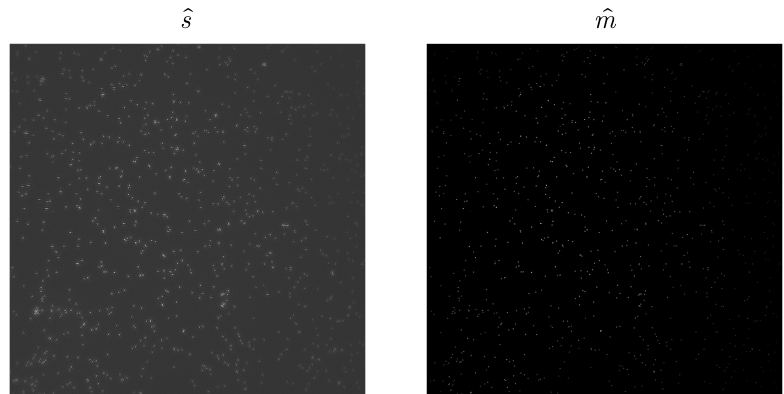


Figure 4.16: The reconstructed HR image and the final model of the source.

4.4 Estimating the PSF from the Model

The estimate of the degradation function, which for an invariant (aplanatic) system corresponds to the transfer function, supported that we have a source model and its acquisition can be made very trivially [35]. If we write the noisy transfer in the Fourier domain, we get

$$F(\vec{k}) = H(\vec{k}) \cdot S(\vec{k}) + N(\vec{k}), \quad (4.9)$$

where H is the transfer what we want to estimate. Therefore in a noisy acquisition if N is sufficiently small relative to $H \cdot S$, the SNR is sufficiently large, then

$$\frac{F(\vec{k})}{S(\vec{k})} \approx H(\vec{k}).$$

Thus, if we have the model of the source $\hat{m} \approx s$, it is sufficient to make the Fourier transform and pixel-wise division with the sensed image in the Fourier domain and we have an estimate \hat{H} of the OTF.

[35]: Gonzalez (2008), *Image Restoration and Reconstruction*

4.5 PSF from SIM

Since our terminal goal is to perform the SIM reconstruction using the transfer function, we can use the model \hat{m} , and a similar optimization problem as in Section 3.3 and try to determine the best transfer function specifically for this purpose. The optimization problem given a model \hat{m} of the source, given as

$$\hat{H} = \arg \min_H \ell[f, \mathcal{D}[H]], \quad (4.10)$$

The only change from \mathcal{D} in Subsection 3.3 in Equation 4.10 is that now we view the H as the variable instead of the source s and we substitute the source in the forward mapping \mathcal{D} by \hat{m} . We can use the same loss ℓ in Equation 4.10 as in Subsection 3.3. It is not necessary to perform regularization if instead of the OTF H the optimization done for the PSF h which can be sampled over a small region and therefore we can avoid the optimization problem to be underspecified, since we have many more data points within the data f than we want to optimize over in the PSF h .

4.6 Revised Reconstruction

There is a possibility of enhancing the reconstruction at a give location by using the transfer function from that location instead of a model estimate from the whole image plane. In this spirit the image was subdivided into patches of right-top, left-top, center-center, right-bottom and left-bottom in the xy -plane. 12 beads were selected from each patch within the image. An averaging estimation of the PSF was performed and the Wiener filter reconstruction of the full image plane was made using the localized PSF.

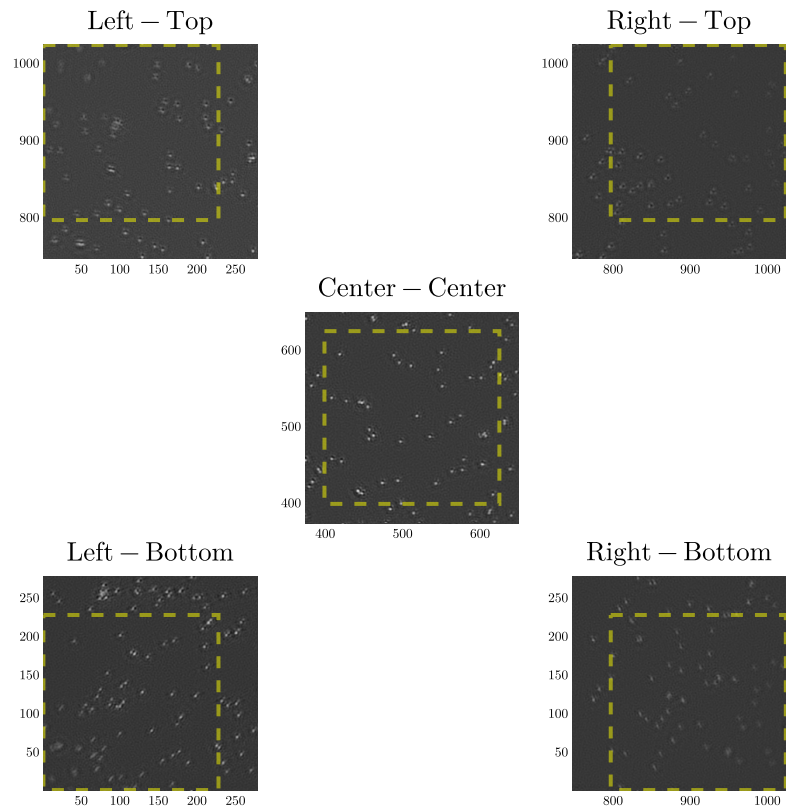


Figure 4.17: The reconstructions of the image using the localized PSF estimates. Boxes indicate the patches, where the beads, were selected from for the PSF estimate.

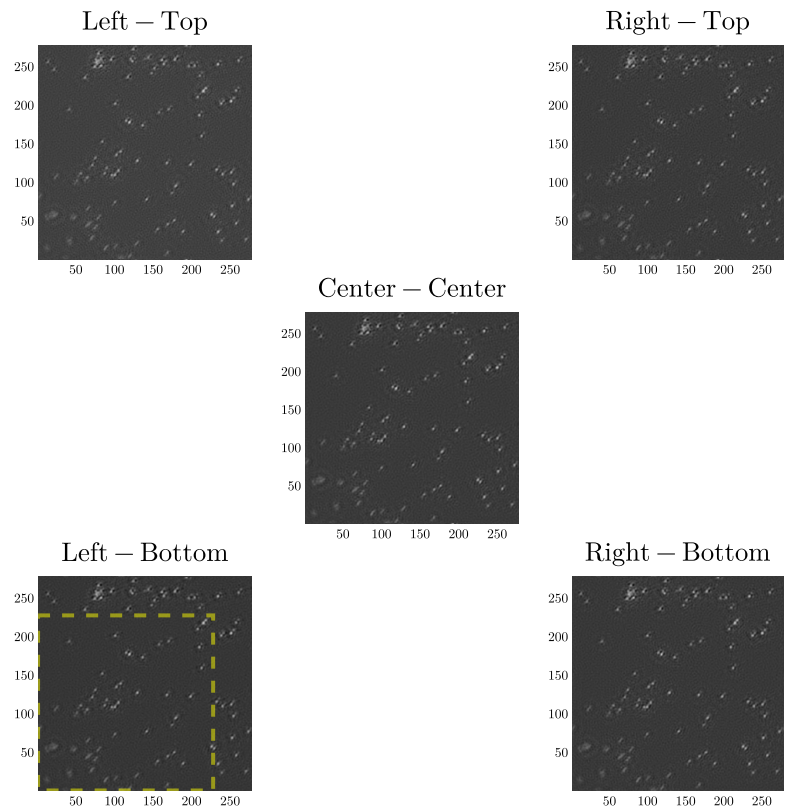


Figure 4.18: Comparison of the left-bottom patch using the reconstructions of the image using the localized PSF estimates. There is a slight visible difference near the edges of the beads.

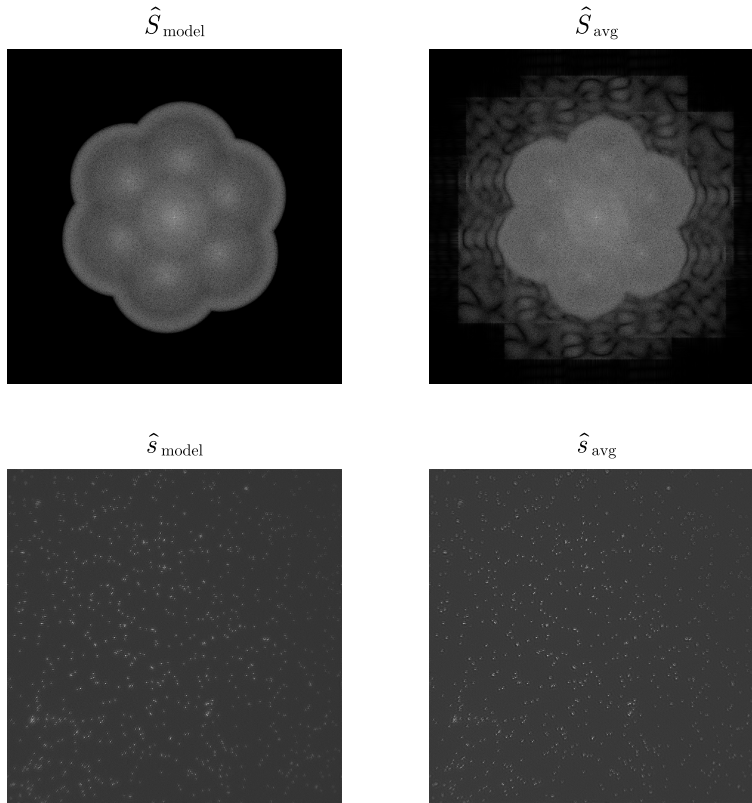


Figure 4.19: Comparison of the reconstructions and their Fourier transforms made using the model OTF and using the center-center patch localized averagedPSF. There is a significant difference in the uniformity of the Fourier image. Moreover, there are no visible peaks in the centres of the components. This reduces the artefacts that are caused by the incorrect transfer function significantly.

There are perceivable differences between the patch reconstructions (Fig. 4.17) using the PSFs estimates from the patches. In general, however, the reconstruction of the image with the patch estimate of the PSF at the patch indices is noticeably better than those with PSF estimate other than that particular patch (Fig. 4.18). It is logical and true that the center patch estimate of the PSF produces reconstructions that are best in average over the whole image plane, since the aberrations are closest to the off-center ones in average.

The next step is to compare the reconstruction using the model and the estimate. This is done in Figure 4.19, where the reconstruction using the center-center patch PSF estimate is shown. A resolution and visual enhancement is undoubtedly achieved using this reconstruction.

We also want to see, if the estimated transfer function is useful for the reconstruction of acquisition of the cell, since this is the prime goal of making these estimates. To assess the quality of the reconstruction, we use the center-center patch PSF and the model OTF to reconstruct cell image SIM acquisition using the same microscope (Fig. 4.20).

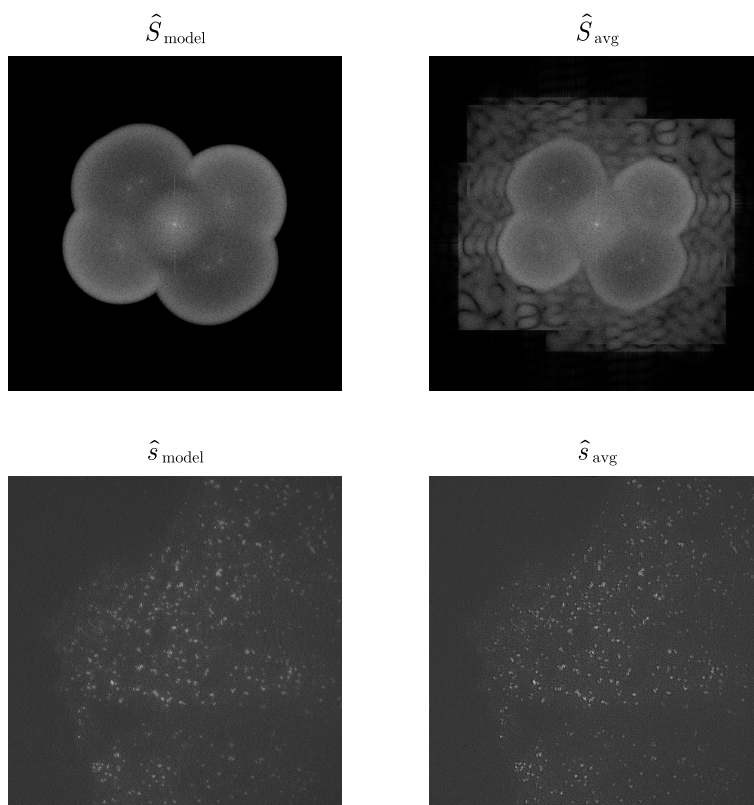


Figure 4.20: A comparison of the reconstruction of the cell acquisition made by the model and the center-center patch estimate of the PSF. A visual quality enhancement is achieved, although based on the Fourier space results, an even better result might be possible by using apodization or limiting estimating the support of the OTF produced by the PSF and artificially reducing it to 0 out of the bound of the support.

The quality improvement is also undeniable, so we may conclude, that the PSF estimate is more adequate for the cell images as well (which is logical). For better comparison of the artefact elimination, a closer view of the reconstruction is shown in Figure 4.21.

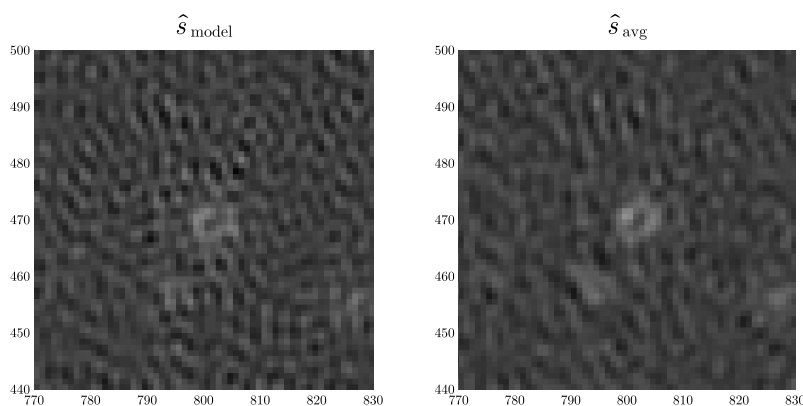


Figure 4.21: A close up of the spatial result achieved using the model and the center-center PSF estimate. Although the artefacts are not fully eliminated a reduction is evident.

4.7 Discussion

Although significant improvement is achieved there is a vast opportunity for improvement. Some of the improvements may be made to the estimation of the PSF itself, but there is also room for enhancing the reconstruction algorithm (Wiener filter is used) to match the attributes of the PSF estimate.

First for the estimation of the PSF.

1. As has been indicated in Subsection 4, the model of the noise is truly the one and discussed in the subsection. There are methods for fitting the model, one of which was cited and commented upon in the subsection. If this fit was to be made, we could calculate the distribution of the estimate of the averaged bead. This could give us the opportunity to optimize the transfer function further, based on the artefacts that are produced by the reconstruction employing it by defining some loss related to the amount of artefacts produced. This optimization could be made with the knowledge of how probable it is for the PSF to truly be this optimized form in contrast to the base estimate.
2. The source model estimation, or more specifically the Subsection 4.3 lead to finding bead locations that were merely artefacts. This could be eliminated by developing a locating algorithm on the LR summed image, which does not include artefacts and the resulting locations could be compared and further filtered to eliminate all the artefacts. It, however, is not possible to distinguish some artefacts from true beads even by eye, so an ideal model is not thinkable using this approach.
3. The PSF metric of full width at half maximum (FWHM) has been found to be different for the center and edge estimated PSFs. This is not a surprise, since we know that the edge locations are more affected by the aberrations. However, it proposes a possibility of determining the aberrations through assessing the OTF produced by the measured PSF through fitting of Zernike polynomials [36] and through this, it may be possible to produce a model of the location variant aberrations strength. This could be utilized to determine a location variant model of the transfer function and improve the model reconstruction.

[36]: Siddik et al. (2023), *Deep Learning Estimation of Modified Zernike Coefficients and Recovery of Point Spread Functions in Turbulence*

More importantly, what is possible to improve in the reconstruction in order of assumed importance:

1. Limiting the support of the OTF that is produced by the PSF which should further reduce the artefacts.
2. Seeing from the Fourier space reconstructions, that the edges of the components are still have a visibly higher intensity than the centres of the components, this could be alleviated by using apodization, which should further reduce the artefacts.
3. The FWHM in x and y axes differed significantly in all the estimations except for the center-center patch estimate. This means that the spherical and coma are present and that the aplanatic assumption is wrong by a greater margin than is expected. The size of the error of the aplanatic assumption is a clear indication, that tiled reconstruction could markedly improve the reconstructions. There is also the possibility of an even better approach than the tiles produced by the estimate from the averaging of beads throughout some predefined patches of the image plane. It is in the assessment and integration of the estimate from Section 4.4, which could produce the estimate for any given sufficiently large window within the image.
4. It is visible that the center components are have a greater intensity than the edge components by a significant amount which is

not realistically the true ratio of intensities. This could be more closely analysed by the Fourier transform of the LR image sum, as there is some overlap between the components. This indicates the wrong estimation of modulations of the illumination patterns. Therefore the modulation estimate should be modified and the resulting reconstruction of those modification should be monitored to assess its influence. If we had a measure for the artefacts, it would even be possible to optimize modulations based on the reconstruction artefacts, it produces.

Summary and Conclusion

I have demonstrated various different methods of the SIM reconstruction from images of an acquisition using structured illumination. Two algorithms for reconstruction, the Wiener filter and the optimization reconstructions in several forms and modifications were presented, implemented and their results were presented compared and a commentary was given as to their drawbacks and benefits. There were given options and prospects for improvement upon these algorithms that should lead to further enhancing the results achieved. Also, a demonstration of the possibility of use of a reduced number of acquisitions was made, that was commented upon in the literature, but the results were previously not presented.

A faithful image formation model was developed in the context of the pursuit of estimating the transfer function of the optical system. The theoretical sources of noise were discussed, before a model of the noise was stated and its validity was indicated. Then a procedure for estimating the PSF from a specific acquisition of micro-spheres (beads) was presented and realized. Then a model of the source of the acquisition was developed via a custom algorithm inspired by other image processing algorithms with a result that is well justified by the sensed image. Two other possible methods of estimating the transfer function were presented and implemented, one inspired by the optimization reconstruction algorithm, with the use of the source model developed and the other also via the source model, but by use of the LR image sum. The averaging of beads estimation was realized on different patches of the image plane and comparison of the reconstructions made using the estimates was demonstrated. Finally the validity and justification for use of these estimations was demonstrated by a reconstruction of the cell using the estimate. A thorough discussion was given on the possible improvements upon the algorithms used.

The final reconstruction of the cell using the estimate demonstrates a compelling result with a visible improvement in the quality, artefacts partially eliminated and the structure of the clathrin-coated pits (CCPs) on the cell membrane surface visible in better contrast against the background noise. I have demonstrated the validity of the procedures developed and the achieved results improvement is unmistakable. Future possibilities for and paths towards improvement are clearly stated.

Bibliography

- [1] Dominique Raynaud. *A Critical Edition of Ibn al-Haytham's On the Shape of the Eclipse: The First Experimental Study of the Camera Obscura*. 1st ed. 2016 edition. New York, NY: Springer, Nov. 25, 2016. 323 pp. (cited on page 4).
- [2] Isaac Newton. *Opticks, Or, A Treatise of the Reflections, Refractions, Inflections & Colours of Light*. 1st ed. 1704. 546 pp. (Visited on 11/07/2023) (cited on page 4).
- [3] Joseph W. Goodman. 'Foundations of Scalar Diffraction Theory'. In: *Introduction to Fourier Optics*. 3rd ed. Englewood, Colo: Roberts & Co, 2005 (cited on page 5).
- [4] Richard P. Feynman, Leighton, and Sands. *Feynman Lectures on Physics, Vol. II: The New Millennium Edition: Mainly Electromagnetism and Matter*. New Millennium ed. edition. New York: Basic Books, Oct. 4, 2011. 589 pp. (cited on page 6).
- [5] Francois Aguet. 'Super-Resolution Fluorescence Microscopy Based on Physical Models'. EPFL Thesis no. 4418 (2009), 209 p. École polytechnique fédérale de Lausanne (EPFL), May 28, 2009. 209 pp. (Visited on 07/08/2023) (cited on pages 9, 37).
- [6] Christoph Cremer and Thomas Cremer. 'Considerations on a Laser-Scanning-Microscope with High Resolution and Depth of Eld'. In: *Microsc. Acta*. 81 (Oct. 1, 1978) (cited on pages 12, 14).
- [7] John M. Guerra. 'Super-Resolution through Illumination by Diffraction-Born Evanescent Waves'. In: *Applied Physics Letters* 66.26 (June 26, 1995), pp. 3555–3557. DOI: [10.1063/1.113814](https://doi.org/10.1063/1.113814). (Visited on 01/07/2024) (cited on pages 12, 14).
- [8] Rainer Heintzmann and Christoph G. Cremer. 'Laterally Modulated Excitation Microscopy: Improvement of Resolution by Using a Diffraction Grating'. In: *Optical Biopsies and Microscopic Techniques III*. Optical Biopsies and Microscopic Techniques III. Vol. 3568. Stockholm, Sweden: SPIE, Jan. 19, 1999, pp. 185–196. DOI: [10.1117/12.336833](https://doi.org/10.1117/12.336833). (Visited on 07/08/2023) (cited on pages 12, 14).
- [9] Paul S. Weiss. 'Nobel Prizes for Super-Resolution Imaging'. In: *ACS Nano* 8.10 (Oct. 28, 2014), pp. 9689–9690. DOI: [10.1021/nm505967q](https://doi.org/10.1021/nm505967q). (Visited on 07/08/2023) (cited on page 12).
- [10] Amit Lal, Chunyan Shan, and Peng Xi. 'Structured Illumination Microscopy Image Reconstruction Algorithm'. In: *IEEE Journal of Selected Topics in Quantum Electronics* 22.4 (July 2016), pp. 50–63. DOI: [10.1109/JSTQE.2016.2521542](https://doi.org/10.1109/JSTQE.2016.2521542) (cited on page 12).
- [11] Ahmet Yildiz et al. 'Myosin V Walks Hand-Over-Hand: Single Fluorophore Imaging with 1.5-Nm Localization'. In: *Science* 300.5628 (June 27, 2003), pp. 2061–2065. DOI: [10.1126/science.1084398](https://doi.org/10.1126/science.1084398). (Visited on 01/07/2024) (cited on page 14).
- [12] Stefan W. Hell and Jan Wichmann. 'Breaking the Diffraction Resolution Limit by Stimulated Emission: Stimulated-Emission-Depletion Fluorescence Microscopy'. In: *Optics Letters* 19.11 (June 1, 1994), p. 780. DOI: [10.1364/OL.19.000780](https://doi.org/10.1364/OL.19.000780). (Visited on 01/07/2024) (cited on page 14).
- [13] Eric Betzig et al. 'Imaging Intracellular Fluorescent Proteins at Nanometer Resolution'. In: *Science* 313.5793 (Sept. 15, 2006), pp. 1642–1645. DOI: [10.1126/science.1127344](https://doi.org/10.1126/science.1127344). (Visited on 01/07/2024) (cited on page 14).
- [14] Michael J Rust, Mark Bates, and Xiaowei Zhuang. 'Sub-Diffraction-Limit Imaging by Stochastic Optical Reconstruction Microscopy (STORM)'. In: *Nature Methods* 3.10 (Oct. 2006), pp. 793–796. DOI: [10.1038/nmeth929](https://doi.org/10.1038/nmeth929). (Visited on 01/07/2024) (cited on page 14).
- [15] Sheema Rahmanseresht et al. 'Pushing the Boundary of Storm Resolution: Seeing the Actin Lattice in Muscle'. In: *Biophysical Journal* 114.3 (Feb. 2018), 13a. DOI: [10.1016/j.bpj.2017.11.117](https://doi.org/10.1016/j.bpj.2017.11.117). (Visited on 01/07/2024) (cited on page 14).
- [16] Mats G. L. Gustafsson et al. 'Three-Dimensional Resolution Doubling in Wide-Field Fluorescence Microscopy by Structured Illumination'. In: *Biophysical Journal* 94.12 (June 15, 2008), pp. 4957–4970. DOI: [10.1529/biophysj.107.120345](https://doi.org/10.1529/biophysj.107.120345). (Visited on 07/08/2023) (cited on pages 14, 17).

- [17] Li-Hao Yeh, Lei Tian, and Laura Waller. ‘Structured Illumination Microscopy with Unknown Patterns and a Statistical Prior’. In: *Biomedical Optics Express* 8.2 (Feb. 1, 2017), pp. 695–711. DOI: [10.1364/B0E.8.000695](https://doi.org/10.1364/B0E.8.000695). (Visited on 07/08/2023) (cited on page 17).
- [18] E. Mudry et al. ‘Structured Illumination Microscopy Using Unknown Speckle Patterns’. In: *Nature Photonics* 6.5 (5 May 2012), pp. 312–315. DOI: [10.1038/nphoton.2012.83](https://doi.org/10.1038/nphoton.2012.83). (Visited on 07/08/2023) (cited on page 17).
- [19] Mats G. L. Gustafsson. ‘Nonlinear Structured-Illumination Microscopy: Wide-field Fluorescence Imaging with Theoretically Unlimited Resolution’. In: *Proceedings of the National Academy of Sciences* 102.37 (Sept. 13, 2005), pp. 13081–13086. DOI: [10.1073/pnas.0406877102](https://doi.org/10.1073/pnas.0406877102). (Visited on 07/08/2023) (cited on page 17).
- [20] E. Hesper Rego et al. ‘Nonlinear Structured-Illumination Microscopy with a Photoswitchable Protein Reveals Cellular Structures at 50-Nm Resolution’. In: *Proceedings of the National Academy of Sciences* 109.3 (Jan. 17, 2012), E135–E143. DOI: [10.1073/pnas.1107547108](https://doi.org/10.1073/pnas.1107547108). (Visited on 12/17/2023) (cited on page 18).
- [21] Xiaoshuai Huang et al. ‘Fast, Long-Term, Super-Resolution Imaging with Hessian Structured Illumination Microscopy’. In: *Nature Biotechnology* 36.5 (5 May 2018), pp. 451–459. DOI: [10.1038/nbt.4115](https://doi.org/10.1038/nbt.4115). (Visited on 07/08/2023) (cited on page 23).
- [22] Patrick K Mogensen and Asbjørn N Riseth. ‘Optim: A Mathematical Optimization Package for Julia’. In: *Journal of Open Source Software* 3.24 (Apr. 4, 2018), p. 615. DOI: [10.21105/joss.00615](https://doi.org/10.21105/joss.00615). (Visited on 01/08/2024) (cited on page 32).
- [23] François Orioux et al. ‘Bayesian Estimation for Optimized Structured Illumination Microscopy’. In: *IEEE Transactions on Image Processing* 21.2 (Feb. 2012), pp. 601–614. DOI: [10.1109/TIP.2011.2162741](https://doi.org/10.1109/TIP.2011.2162741) (cited on page 33).
- [24] David P. Hoffman and Eric Betzig. *Tiled Reconstruction Improves Structured Illumination Microscopy*. preprint. Cell Biology, Jan. 6, 2020. DOI: [10.1101/2020.01.06.895318](https://doi.org/10.1101/2020.01.06.895318). (Visited on 07/07/2023) (cited on page 34).
- [25] Joseph W. Goodman. ‘Phase Retrieval from Fourier Magnitude’. In: *Introduction to Fourier Optics*. 3rd ed. Englewood, Colo: Roberts & Co, 2005, pp. 38–39 (cited on page 35).
- [26] Bridget M. Hanser et al. ‘Phase Retrieval for High-Numerical-Aperture Optical Systems’. In: *Optics Letters* 28.10 (May 15, 2003), pp. 801–803. DOI: [10.1364/OL.28.000801](https://doi.org/10.1364/OL.28.000801). (Visited on 07/08/2023) (cited on page 35).
- [27] Samuel W. Hasinoff. ‘Photon, Poisson Noise’. In: *Computer Vision: A Reference Guide*. Ed. by Katsushi Ikeuchi. 2nd ed. 2021 edition. Springer, Sept. 30, 2021, pp. 980–982 (cited on page 37).
- [28] G. Holst. ‘Scientific CMOS Camera Technology: A Breeding Ground for New Microscopy Techniques’. In: 2014. (Visited on 07/09/2023) (cited on page 37).
- [29] Nobuyuki Otsu. ‘A Threshold Selection Method from Gray-Level Histograms’. In: *IEEE Transactions on Systems, Man, and Cybernetics* 9.1 (Jan. 1979), pp. 62–66. DOI: [10.1109/TSMC.1979.4310076](https://doi.org/10.1109/TSMC.1979.4310076) (cited on page 38).
- [30] A. Foi et al. ‘Practical Poissonian-Gaussian Noise Modeling and Fitting for Single-Image Raw-Data’. In: *IEEE Transactions on Image Processing* 17.10 (Oct. 2008), pp. 1737–1754. DOI: [10.1109/TIP.2008.2001399](https://doi.org/10.1109/TIP.2008.2001399). (Visited on 12/29/2023) (cited on page 38).
- [31] Nicolas Bahler et al. ‘PoGaIN: Poisson-Gaussian Image Noise Modeling From Paired Samples’. In: *IEEE Signal Processing Letters* 29 (2022), pp. 2602–2606. DOI: [10.1109/LSP.2022.3227522](https://doi.org/10.1109/LSP.2022.3227522). (Visited on 12/28/2023) (cited on page 39).
- [32] Rachel Smith. *TetraSpeck™ microspheres, 0.1µm - Certificate of Analysis*. Oct. 8, 2020. URL: <https://www.thermofisher.com/document-connect/document-connect.html?url=https://assets.thermofisher.com/TFS-Assets%2FBIOD%2Fcertificate%2FCertificates-of-Analysis%2FT7279%20Lot%202273691%20CoFA.pdf> (visited on 07/20/2023) (cited on page 41).

- [33] Rafael C. Gonzalez. ‘Fundamentals of Spatial Filtering’. In: Rafael C. Gonzalez and Richard E. Woods. *Digital Image Processing*. 3. ed., internat. ed. Pearson Education. Upper Saddle River, NJ: Pearson Education Internat, 2008, pp. 144–151 (cited on page 45).
- [34] Rafael C. Gonzalez. ‘Morphological Image Processing’. In: Rafael C. Gonzalez and Richard E. Woods. *Digital Image Processing*. 3. ed., internat. ed. Pearson Education. Upper Saddle River, NJ: Pearson Education Internat, 2008, pp. 627–688 (cited on page 46).
- [35] Rafael C. Gonzalez. ‘Image Restoration and Reconstruction’. In: Rafael C. Gonzalez and Richard E. Woods. *Digital Image Processing*. 3. ed., internat. ed. Pearson Education. Upper Saddle River, NJ: Pearson Education Internat, 2008, pp. 311–393 (cited on page 47).
- [36] Abu Bucker Siddik et al. ‘Deep Learning Estimation of Modified Zernike Coefficients and Recovery of Point Spread Functions in Turbulence’. In: *Optics Express* 31.14 (July 3, 2023), pp. 22903–22913. DOI: [10.1364/OE.493229](https://doi.org/10.1364/OE.493229). (Visited on 11/27/2023) (cited on page 51).

List of Acronyms and Abbreviations

| | | |
|---------------------------|---|---|
| 4πM | 4 π -microscopy | 1, 12, 14 |
| CCP | clathrin-coated pit | 53 |
| CMOS | complementary metal–oxide–semiconductor | 35–37 |
| DFT | discrete Fourier transform | 28 |
| EM | electro-magnetic | 7, 4–8, 11, 35 |
| FIONA | fluorescence imaging with one-nanometer accuracy | 14 |
| FM | fluorescent microscopy | 6, 8 |
| FWHM | full width at half maximum | 51 |
| GR | Good’s roughness | 31, 32 |
| HR | high-resolution | 20, 24–28, 42–46 |
| ID | identification | 16 |
| L-BFGS | limited-memory Broyden–Fletcher–Goldfarb–Shanno | 31 |
| LCD | liquid-crystal display | 15 |
| LED | light-emitting diode | 15 |
| LR | low-resolution | 20–22, 24–26, 29, 30, 33, 34, 42–44, 46, 51, 53 |
| LSE | least square error | 41 |
| MLE | maximum likelihood estimate | 30, 38 |
| OTF | optical transfer function | 17, 20, 22, 23, 25–29, 35, 40, 47, 49, 51 |
| PALM | photo-activated localization microscopy | 14 |
| PSF | point spread function | 27, 29, 35, 40–44, 47, 49–51, 53 |
| ROI | region of interest | 45, 46 |
| SI | Système International | 5 |
| SIM | structured illumination microscopy | 7, 1, 12–17, 20, 22, 24, 26, 28, 30, 32, 34, 35, 47, 49, 53 |
| SNR | signal-to-noise ratio | 27, 30, 36, 47 |
| SR | super-resolution | 7, 1, 12–15 |
| STED | stimulated emission depletion | 12, 14 |
| STORM | stochastic optical reconstruction microscopy | 14, 17 |
| TIR | total internal reflection | 43 |
| TIRFM | total internal reflection fluorescence microscopy | 17, 37 |
| TV | total variation | 31, 32 |